CARDIFF UNIVERSITY
PRIFYSGOL CAERDYDD

ORCA – Online Research @ Cardiff

This is an Open Access document downloaded from ORCA, Cardiff University's institutional repository:https://orca.cardiff.ac.uk/id/eprint/159422/

This is the author's version of a work that was submitted to / accepted for publication.

Citation for final published version:

Martin, Andrew J., McDonald, Iain, Jamieson, John W., Jenkin, Gawen R. T., McFall, Katie A., Piercey, Glenn, MacLeod, Christopher J. and Layne, Graham D. 2021. Mineral-scale variation in the trace metal and sulfur isotope composition of pyrite: implications for metal and sulfur sources in mafic VMS deposits. Mineralium Deposita 57 (6) , pp. 911-933. 10.1007/s00126-021-01080-1 file

Publishers page: http://dx.doi.org/10.1007/s00126-021-01080-1

Please note:
Changes made as a result of publishing processes such as copy-editing, formatting and page numbers may not be reflected in this version. For the definitive version of this publication, please refer to the published source. You are advised to consult the publisher's version if you wish to cite this paper.

This version is being made available in accordance with publisher policies. See http://orca.cf.ac.uk/policies.html for usage policies. Copyright and moral rights for publications made available in ORCA are retained by the copyright holders.

Mineral-scale variation in the trace metal and sulfur isotope composition of pyrite: Implications for metal and sulfur sources in mafic VMS deposits

Andrew J. Martin[1*], Iain McDonald[2], John W. Jamieson[1], Gawen R.T. Jenkin[3], Katie A. McFall[1], Glenn Piercey[4], Christopher J. MacLeod[1] and Graham D. Layne[1]

[1]Department of Earth Sciences, Memorial University of Newfoundland, Canada

[2]School of Earth and Environmental Sciences, Cardiff University, UK

[3]School of Geography, Geology and the Environment, University of Leicester, UK

[4]MAF-IIC SIMS Facility, Memorial University of Newfoundland, Canada

[*] Corresponding author: ajmartin@mun.ca

Abstract

The link between metal enrichment and the addition of a magmatic volatile phase in volcanogenic massive sulfide deposits and actively forming seafloor massive sulfide deposits remains poorly characterized. This is especially true when considering how metal, sulfur and fluid flux change with time. In this study we combine *in situ* sulfur isotope ($\delta^{34}S$; n=31) measurements with trace metal chemistry of pyrite (n=143) from the Mala VMS deposit, Troodos, Cyprus. The aim of our study is to assess the links between volatile influx and metal enrichment and establish how, or indeed if, this is preserved at the scale of individual mineral grains. We classify pyrite based on texture into colloform, granular, disseminated and massive varieties. The trace metal content of different pyrite textures is highly variable and relates to fluid temperature and secondary reworking that are influenced by the location of the sample within the mound. The sulfur isotope composition of pyrite at Mala ranges from -17.1 to 7.5‰ (n=31), with a range of -10.9 to 2.5‰ within a single pyrite crystal. This variation is attributed to changes in the relative proportion of sulfur sourced from i) SO_2 disproportionation, ii) thermochemical sulfate reduction, iii) the leaching of igneous sulfur/sulfide and, iv) bacterial sulfate reduction. Our data shows that there is no correlation between $\delta^{34}S$ values and the

concentration of volatile elements (Te, Se) and Au in pyrite at Mala indicating that remobilization of trace metals occurred within the mound.

Introduction

The source of metals in volcanogenic massive sulfide (VMS) and actively forming seafloor massive sulfide (SMS) deposits remains poorly constrained and actively debated (Sillitoe et al. 1996; Yang and Scott 1996; Jowitt et al. 2012; Keith et al. 2018; Martin et al. 2020; Patten et al. 2020). Principally, two metal sources can contribute to the metal budget of VMS deposits: leaching of metals from underlying host rocks during hydrothermal alteration (Richardson et al. 1987; Jowitt et al. 2012; Banerjee et al. 2000; Patten et al. 2017); and the addition of a magmatic volatile phase to the overlying hydrothermal system (Yang and Scott 1996, 2002; de Ronde et al. 2011; Martin et al. 2020, 2021; Patten et al. 2020). The relative contribution of metals from these two sources and how they change with system maturity (i.e. time) and the subsequent preservation of trace metal signatures to distinguish these sources in sulfide minerals in VMS deposits remains enigmatic. Here, we apply *in situ* geochemical and sulfur isotope measurements on pyrite from the 92 million year old Mala VMS deposit of the Troodos ophiolite (Cyprus) to assess co-variations in trace metal content and sulfur isotope ratios ($\delta^{34}S$) in an ancient mafic VMS deposit. These data will be used to investigate the variability in metal and sulfur sources during the growth of individual pyrite crystals and to understand if the influx of certain volatile metals can be linked to variations in sulfur isotopic composition.

To investigate the source(s) of metals in VMS deposits, previous studies utilized either trace metal enrichment profiles (Halbach et al. 1998; Butler and Nesbitt 1999; Maslennikov et al. 2009; Wohlgemuth-Ueberwasser et al. 2015; Keith et al. 2016a; Grant et al. 2018; Wang et al. 2018), the ratio of Se to S (Yamamoto 1976; Huston et al. 1995; Hannington et al. 1999; Layton-Matthews et al. 2008, 2013; Martin et al. 2019), or the sulfur isotopic composition of sulfide minerals (Herzig et al. 1998; Gemmell et al. 2004; Huston et al. 2011; Yeats et al. 2014; Brueckner et al. 2015; Lode et al. 2017; Zeng et al. 2017). However, very few studies utilize a combined approach (e.g., Rouxel et al. 2004; Sharman et al. 2015; Meng et al.

2020; Martin et al. 2021) that takes into consideration any systematic relationship between trace element enrichment profiles and the sulfur isotopic composition of sulfide minerals; this is especially true when considering the complex nature of different pyrite textures, generations (i.e. overgrowths) and variation that occurs at the scale of individual mineral grains.

In volatile-rich, subduction influenced VMS deposits, the systematic enrichment of certain metals such as Pb, As, Sb, Bi, Hg and Te (Wohlgemuth-Ueberwasser et al. 2015), Se, Cu and Te (Keith et al. 2016a), Bi and Te (Mathieu 2019) or Se, Cu, Te and Au (Martin et al. 2021) have been proposed to indicate the addition of a metal-rich magmatic volatile phase to the hydrothermal system from degassing of shallow magma reservoirs (e.g., Huston et al. 2011). Additionally, elevated Se/S (expressed as $Se/S*10^6$) that are >500 in pyrite are also interpreted as representing an increased magmatic volatile influx in VMS deposits (Yamamoto 1976; Huston et al. 1995; Layton-Matthews et al. 2008, 2013). The sulfur isotopic composition of sulfide minerals provides further evidence of a magmatic volatile contribution to VMS deposits with the addition of degassing magmatic SO_2 that undergoes disproportionation upon mixing with hydrothermal fluid, and results in a characteristic sulfur isotope composition defined by $\delta^{34}S$ values that are less than the magmatic mean (<0‰, MORB; Herzig et al. 1998; Kusakabe et al. 2000; de Ronde et al. 2005). These low $\delta^{34}S$ values are generally limited to felsic or subduction influenced environments (e.g., Herzig et al. 1998; Huston et al. 2011), where magmas are more volatile-rich relative to mafic hosted mid-ocean ridge (MOR) environments (Wallace 2005). However, this signature was also recorded in an ancient mafic VMS deposit (Martin et al. 2021). This sulfur isotope composition contrasts signatures typical of MOR environments, where $\delta^{34}S$ values in sulfide minerals are positive, indicating a combination of sulfur from thermochemical sulfate reduction (TSR) of seawater at high temperatures (>160°C) in the presence of iron-bearing minerals and leaching of sulfur and primary igneous sulfide minerals from igneous host rocks (Ono et al. 2007).

Previous studies utilising laser ablation inductively coupled plasma mass spectrometry (LA-ICP-MS) of sulfide minerals from Troodos VMS deposits indicate that deposits associated with the Solea graben, one of three fossil spreading axes in the Troodos ophiolite are enriched in Se, Cu and Au (Keith et al. 2016a;

Fig. 1). The enrichment of these elements is attributed to the contribution of a magmatic volatile phase to the hydrothermal systems of the Solea graben (Martin et al. 2019, 2020).

Variation in the sulfur isotope composition of pyrite has largely been constrained in Troodos VMS deposits using whole-rock analytical methods of sulfide minerals with the median composition for all Troodos VMS sulfide minerals of 4.6±2.7‰ (1σ, n=220) indicating that sulfur is primarily sourced from both the leaching of igneous sulfur/sulfide and TSR of seawater (Hannington et al. 1998; Parvaz 2014; Keith et al. 2016a; Pedersen et al. 2017; Martin et al. 2020). However, significant variation is noted in the sulfur isotope composition of pyrite across Troodos VMS deposits with the $\delta^{34}S$ values of pyrite ranging from -7.6‰ to 13.2‰ (Martin et al. 2020, 2021). Samples of disseminated pyrite that occur within the volcanic stratigraphy exhibit significantly lower $\delta^{34}S$ values than those typical for Troodos VMS deposits; pyrite is depleted in ^{34}S, with $\delta^{34}S$ values ranging from -22.2‰ to -6.9‰. These values indicate that bacterial sulfate reduction (BSR) occurred at low temperatures (<120°C) in the shallow subsurface, away from areas of high temperature fluid discharge (Pedersen et al. 2017).

Sulfide mineral chemistry and the sulfur isotopic composition of sulfide minerals analysed using bulk analytical techniques leads to the homogenization of any variation in the chemical and isotopic composition of the sample. Thus, there is a need to apply *in situ* analytical techniques to better understand the spatial zonation in isotopic and chemical composition within individual mineral grains. Utilizing a combined approach of *in situ* LA-ICP-MS analysis to measure trace metal concentrations and Secondary Ion Mass Spectrometry (SIMS) to measure sulfur isotope ratios, this study aims to establish if links exist between trace metal enrichment and variations in the source of sulfur during VMS deposit formation. We focus on the Mala VMS deposit located in the Troodos ophiolite of Cyprus, as Mala represents an immature magmatic volatile-influenced deposit where links between magmatic volatile influx, sulfur isotope ratios and trace metal enrichment signatures in pyrite have not been extensively modified during fluid overprinting associated with the maturation of the VMS mound (Martin et al. 2021). We present *in situ* sulfur isotope data and trace element geochemistry of different pyrite textures that highlight variable trace

element enrichment profiles that can be related to mound-scale fluid flow. We then combine trace metal geochemistry and sulfur isotope ratios to test if any systematic relationship exists between magmatic volatile influx and the enrichment of Te, Se and Au in pyrite at Mala.

Geological Setting

The 92 Ma Troodos ophiolite in Cyprus comprises a complete, un-deformed oceanic pseudo-stratigraphy (Gass 1968; Mukasa and Ludden 1987). Mantle peridotites are surrounded radially by gabbro and plagiogranite of the plutonic sequence, a sheeted dyke complex (SDC), and the basal group (BG), which consists of a transitional horizon between the SDC and overlying upper and lower pillow lavas (UPL-LPL; Fig. 1) (Gass 1968). It has long been recognized that the Troodos ophiolite formed in a sediment-free subduction influenced environment due to the occurrence of boninite (Pearce and Robinson 2010; Woelki et al. 2018), the trace element and isotopic composition of volcanic glass (Rautenschlein et al. 1985), elevated H_2O contents of parent melts (>2 wt.% H_2O; Muenow et al. 1990), and an enrichment of magmatic volatile derived elements (e.g., Te, Se) in some VMS deposits (Keith et al. 2016b; Martin et al. 2019, 2021).

Observations from actively forming intermediate to slow seafloor spreading centers are akin to processes and structures preserved in the Troodos ophiolite (Varga and Moores 1985). On the northern flank of the ophiolite, three structural grabens are delineated by inversely dipping sheeted dykes along a series of ~north-south normal faults (Varga and Moores 1985). The grabens from east to west are; Larnaca, Mitsero and Solea (Fig. 1). The grabens are widely accepted as representing fossil axial spreading ridges (Varga and Moores 1985). Associated with these graben bounding faults are VMS deposits that formed within or at the contact between the BG, LPL and UPL units at the periphery of the ophiolite that once represented the Cretaceous seafloor (Hannington et al. 1998; Adamides 2010; Fig. 1).

Hydrothermal alteration of the Troodos crust is well-characterized and the leaching of metals from the SDC during spilitisation and epidosite formation is interpreted as a possible source of metal and sulfur in overlying VMS deposits (Richardson et al. 1987; Jowitt et al. 2012; Patten et al. 2017). More recently, a

pulsed magmatic volatile component has been suggested as an additional source of some metals (Cu, Au, Te and Se) in Troodos VMS deposits, especially in magmatic volatile-influenced VMS deposits such as Mala and deposits associated with the Solea graben in particular (Keith et al. 2016a; Martin et al. 2020; Fox et al. 2020).

The Mala VMS deposit

The Mala VMS deposit is located in the southwest Troodos ophiolite, northwest of the town of Pano Pangia within the Pafos Forest region (Fig. 1). Mala is located deep in the lava stratigraphy at the BG-LPL transition. Previous studies have identified an enrichment in Te, Se, Cu and Au in pyrite at Mala relative to other Troodos VMS deposits (Martin et al. 2021). Mala has been historically mined for Cu and Zn (0.8 Mt total; Brazilian Metals Group, 2013) leading to the exposure of a massive sulfide mound at the northern end of the open pit (Fig. 2).

The exposed pyrite mound measures approximately 12 x 8 m (width x height) and contains pyrite and gypsum (Fig. 2A). Gypsum occurs as three distinct morphologies: massive-bedded, breccia infill, and mesh textured varieties (Fig. 2B-G). Within the gypsum are euhedral pyrite crystals which vary in size from <1 mm up to 2 cm in width (Fig. 2D-G). In the VMS mound pyrite forms as five distinct textures: massive euhedral grains (Fig. 3A), dendritic growths (Fig. 3B and C), colloform bands (Fig. 3D), granular pyrite (Fig 3E) and as disseminated grains within gypsum and the surrounding wall rock (Fig. 3F). A previous study by Martin et al. (2021) demonstrated that the pyrite-gypsum relationships preserved at Mala are analogous to those observed in actively forming SMS deposits and reflect primary hydrothermal processes and are not the result of supergene weathering during uplift and exposure.

Methods

Mineral Chemistry

Laser ablation ICP-MS was used to determine *in situ* trace element concentrations in pyrite. Spot analyses (n=143) were performed on 10 representative polished blocks. Analyte masses used were ^{57}Fe, ^{65}Cu, ^{59}Co,

^{66}Zn, ^{75}As, ^{77}Se, ^{109}Ag, ^{111}Cd, ^{121}Sb, ^{125}Te, ^{185}Re, ^{189}Os, ^{193}Ir, ^{195}Pt, ^{197}Au ^{206}Pb and ^{209}Bi (Table S1, ESM). Data were collected using a New Wave Research UP213 laser coupled to a Thermo iCAP RQ-ICP-MS at Cardiff University, UK. Samples were analysed in time-resolved analysis mode with a nominal spot diameter of 55 µm at a frequency of 10 Hz. Each analysis lasted 40 s and a gas blank was measured for 20 s prior to each analysis. Data correction and the subtraction of gas blanks was performed using Thermo Qtegra software. External calibration was performed on a series of synthetic NiFeS standards (see Prichard et al. 2013; Smith et al. 2016) and the reproducibility of analyses was monitored through the repeat analysis of UQAC FeS-1. The repeat analysis of UQAC FeS-1 yielded a relative standard deviation (RSD) of <10% for Fe, Co, Ni, As, Ru, Rh, Pd, Ag, Re, Os, Ir, Pt, Au and Bi, <15% for Cu, Se, Sb and Te and <20% for Zn and Pb. The RSD for Cd was 24% (Table S2, ESM). Detection limits for all elements analysed are available in ESM Table S2. Sulfur-33 was used as an internal standard for all analyses and a stoichiometric concentration of 53.5 wt.% sulfur was used that is within error of the measured average sulfur concentration for pyrite from Troodos VMS deposits (Martin et al. 2019).

Sulfur Isotope analysis

Secondary ion mass spectrometry microanalysis was used to determine the sulfur isotope composition (δ^{34}S) of pyrite. Analysis was undertaken on the same samples analysed via LA-ICP-MS. Epoxy mounted polished blocks (n=6) were first coated with 300Å of Au and were analysed using a Cameca IMS 4f SIMS at the MAF-IIC Microanalysis Facility at Memorial University of Newfoundland following the procedures detailed in Brueckner et al. (2015) and Lode et al. (2017). Systematic analysis of points across pyrite grains was performed proximal to LA-ICP-MS ablation pits to determine variation and correlation between δ^{34}S values and trace element concentrations. The sample was bombarded with a primary ion beam of 350-750 pA of Cs^+, accelerated through a potential of 10 keV and focused into a 5-15 µm diameter spot. The duration of each analyses was 16.3 minutes including 2 minutes of pre-sputtering. To discriminate between $^{33}SH^-$ (and $^{32}SH_2^-$) from $^{34}S^-$ the instrument was operated with a medium contrast aperture (150 µm), with entrance

and exit slits paired to give flat topped peaks at a mass resolving power of 2975 (10% peak height definition; Brueckner et al. 2015). Negatively charged sputtered secondary ions were accelerated into the mass spectrometer using a potential of +4.5 keV. To exclude sulfur contamination from the sample surface the spot was pre-sputtered for 120 s with a 15 µm square rastered beam prior to analysis. Reproducibility based on the repeat analysis of standard reference material pyrite-UL9 ($\delta^{34}S$= 16.3‰) and KH87 ($\delta^{34}S$= 0.4‰), is typically better than ±0.4‰ (1σ) (Table S3, ESM). All analyses are reported in standard notation (‰) relative to Vienna-Canyon Diablo Troilite (V-CDT).

Results

Sample characterization

Samples in this study were collected from the exposed Mala VMS mound (Fig. 2A and Fig. S1, ESM). We subdivide pyrite samples based on texture into massive, dendritic, colloform, granular, and disseminated varieties (Fig. 3). Massive pyrite occurs in discrete meter scale pods consisting of coarse grained (mm to cm) aggregates of euhedral grains (Fig. 2C and 3A and B). Multiple pyrite generations occur as overgrowths within massive pyrite samples and can be delineated by inclusion-rich zones at the grain margin (Fig. 3A). Within massive pyrite, dendritic horizons were common but were not analysed in this study (Fig. 3B and C). Colloform pyrite is rare, occurring spatially associated with granular horizons (Fig. 3D). Granular massive pyrite contains anhedral aggregates of highly resorbed and often spherical pyrite in a pyrite matrix (Fig. 3E). Disseminated pyrite grains are commonly euhedral and vary in size from <1 mm to >2 cm, and occur within gypsum horizons as well as within the volcanic rocks that surround the massive sulfide mound (Fig. 2D and 3F).

Trace element geochemistry

To assess trace metal enrichment profiles, results are grouped based on pyrite texture, and, for disseminated grains, the location of the analytical point in relation to the core or rim of the individual mineral grain that

was analyzed. The division between core and rim is arbitrary and depends on the number of analyses performed within an individual pyrite grain, which in turn reflects the size of the pyrite grain (Table S1, ESM).

Colloform pyrite (n=15) contains the highest median concentrations of Au, Pb and Re at 0.13, 9.8 and 0.17 ppm, respectively. All Ni and Cd analyses are below the detection limit, as are the majority of Cu, Zn and Co (Table 1; Fig. 4A). The concentration of Se is relatively homogenous ranging from 190 to 302 ppm with a median concentration of 245 ppm (n=15) (Fig. 4B, Table 1). The total measured trace metal content for colloform pyrite is 371 ppm (Fig. 4D). A strong positive correlation is noted between Au and Ag (R^2=0.95), and a moderate positive correlation between Pb and Ag (R^2=0.72), Te and Au (R^2=0.56) and Te and Bi (R^2 =0.52).

Granular pyrite (n=10) is depleted in most trace metals relative to other pyrite textures considered here. All analyses for Ni, Ag, Zn, Cd, Re and Pb are below detection limit as are the majority of analyses for Au, Bi, Cu and Sb (Table 1). Cobalt and Te are notably enriched relative to colloform pyrite with median concentrations of 17.9 and 5.9 ppm, respectively (n=10; Fig. 4A; Table 1). As observed in colloform pyrite, the concentration of Se is relatively homogenous, ranging from 5 to 31 ppm, with a median concentration of 6.4 ppm (n=10) (Fig. 4B, Table 1). With the exception of a moderate correlation between As and Se (R^2= 0.63) no notable correlations exist. Granular pyrite contains the lowest measured total trace metal content at 198 ppm (Fig. 4D).

Trace metal enrichment profiles in massive pyrite (n=40) are highly variable between samples. For example, sample MAL 17 is enriched in Cu with a median concentration of 0.04 wt.% with a range of between 0.01 to 0.11 wt.% (n=10) but is relatively depleted in Se with a median concentration of 61 ppm (n=10) (Fig. 4A, Table 1). Across all massive samples, Se exhibits the most variation, ranging from 30 to 1253 ppm with a median concentration of 178 ppm (n=40) (Fig. 4B). With the exception of one point, all analyses for Ni and Cd were below the detection limit (Table 1). Massive pyrite contains the second highest

219 total measured metal content at 566 ppm (Fig. 4D). A weak correlation is noted between Te and Se (R^2 =
220 0.38; Fig. 4B).

221 Grains of disseminated pyrite within gypsum (n=78) contain the highest concentration of Se, Te, As and Bi
222 relative to all other pyrite textures (Fig. 4A-C, Table 1). Trace metal concentrations are highly variable
223 within and between individual samples relative to other pyrite textures analysed in this study. For example,
224 Se concentrations range from 18 to 3261 ppm with a median concentration of 645 ppm (n=78). Similar
225 variability is also noted for Co, As and Te (Table 1; Fig. 4B-C). Sample MAL 05 is notably enriched in Se
226 and Te relative to all other samples with median concentrations of 1668 and 16.4 ppm, respectively (n=14).
227 Disseminated grains have the highest total measured metal content at 981 ppm (Fig. 4D); largely consisting
228 of Se and Cu. Disseminated pyrite grains are sub-divided further based on the location of the analytical
229 point relative to the margin of the pyrite grain to assess metal enrichment trends across individual grains
230 (Fig. 5). With the exception of Co and Cu, that are enriched at the margin of grains (n=43), pyrite cores
231 exhibit a minor enrichment in As, Se, Te and Au relative the grain margins (n=35; Fig. 5).

232 ## Sulfur isotopes

233 Secondary ion mass spectrometry analysis was performed on representative samples of colloform (n=6),
234 granular (n=2), massive (n=9) and disseminated (n=14) textured pyrite (Fig. 6, Table S3, ESM). The median
235 $\delta^{34}S$ value for all samples is -1.2‰ (n=31) with a range of 24.6‰. Granular pyrite exhibits the lightest
236 median sulfur isotopic composition with two analyses yielding $\delta^{34}S$ values of -10.5‰ and -4.7‰. Colloform
237 pyrite consistently exhibits $\delta^{34}S$ values <0‰ ranging from -3.8 to -0.1‰ with a median of -2.2‰ (n=6)
238 (Fig. 6). The sulfur isotopic composition of massive pyrite is highly variable, ranging from -17.1‰ to 7.5‰
239 with a median composition of -1.8‰ (n=9).

240 To assess intra-grain variation in sulfur isotopic composition of disseminated pyrite, transects of analytical
241 points were analysed across different pyrite grains (Fig. 7). The same grains were then etched with NaClO
242 for 90 s to reveal any chemical zonation. A significant amount of variability is recorded in a single pyrite

grain, for example MAL 05 where $\delta^{34}S$ values range from 2.5‰ to -10.9‰ (sub-grain SG1) with a median of 2.0‰ (n=4, Fig. 7A). There is no systematic relationship between $\delta^{34}S$ values and the location of the analysis with respect to the core or rim of the grain, for example, low values do not only occur at the margin of the grain. This is best illustrated in sample MAL 05, an aggregate of three pyrite grains disseminated within gypsum where opposing edges of the pyrite sub-grain SG1 have $\delta^{34}S$ values of -10.9‰ and 2.5‰, respectively (Figure 7A). Individual pyrite grains that are located within the same region of the VMS mound (Fig. 2 and Fig. S1, ESM) also exhibit notable variation, for example two grains from sample MAL 11 (Fig 7B and C) that have different median $\delta^{34}S$ values of -0.9‰ and 0.9‰, respectively (n=7). Again, there is no systematic pattern of enrichment from the grain core to rim within these grains.

Discussion

Mound-scale trace element systematics

The trace metal content and ratio of metals in pyrite can be used as a proxy for the past physical and chemical conditions of hydrothermal fluids (e.g., temperature, pH, fO_2 and fS_2) (Butler and Nesbitt 1999; Hannington et al. 2005; Maslennikov et al. 2009; Genna and Gaboury 2015; Wohlgemuth-Ueberwasser et al. 2015; Keith et al. 2016b; Monecke et al. 2016; Grant et al. 2018; Wang et al. 2018). Thus, variations in trace metal enrichment profiles in pyrite in VMS deposits reflect changes in the physicochemistry of fluids and the flux of metals and fluid entering the VMS deposit during growth of the VMS mound. At the mound scale (~10s of m) steep temperature gradients occur due to variations in the relative amounts of seawater ingress and hydrothermal fluid influx with depth within the mound. Increasing temperatures within the mound lead to the dissolution, recrystallization and remobilization of metals associated with lower temperature sulfide minerals (e.g., Zn, Au, Ag, As, Pb, Sb) from the mound interior to the cooler margin of the mound during zone refining (Eldridge et al. 1983; Hannington et al. 1986; Petersen et al. 2000; Galley et al. 2007). This process is preserved in active SMS deposits as systematic variations in trace metal enrichment profiles between different pyrite textures, such as colloform pyrite that forms near the seawater

interface that is enriched in elements that are associated with low temperature sulfide minerals or those sourced from seawater (e.g., Mo, Tl, Pb; Grant et al. 2018). We note the same systematic variation in the distribution of trace metals between different pyrite textures at the Mala VMS deposit.

Colloform pyrite occurs in active SMS deposits towards the margin of the sulfide mound or during the early stage of chimney growth in environments where seawater ingress is high and fluid temperatures are lower producing non-equilibrium conditions (Maslennikov et al. 2009, 2017; Melekestseva et al. 2014; Wohlgemuth-Ueberwasser et al. 2015; Keith et al. 2016a,b; Grant et al. 2018). Colloform pyrite from Mala is enriched in Au and Pb relative to all other pyrite and contains the lowest median concentration of Co, Cu and Te, with all Ni analyses below detection limit, indicating it formed at lower fluid temperatures. At these low concentrations, both Au and Pb are likely incorporated into the pyrite structure as a lattice bound substitution, whilst at higher concentrations inclusions may occur (Huston et al. 1995; Cook et al. 2009). This trace metal enrichment profile is similar to those reported in colloform pyrite from black smoker chimneys of Urals VMS deposits that are enriched in Au, Ag, Pb and elements derived from seawater such as Mo and Tl that were not analysed in this study (Maslennikov et al. 2009) or colloform pyrite from PACMANUS that is enriched in Au and As but depleted in Te and Se relative to massive pyrite (Wohlgemuth-Ueberwasser et al. 2015). A depletion in Co and Te, which are enriched in high-temperature pyrite varieties (e.g., massive pyrite) in active SMS deposits, further supports a low temperature origin for colloform pyrite at Mala (Wohlgemuth-Ueberwasser et al. 2015; Monecke et al. 2016; Grant et al. 2018). The trace element enrichment profile in colloform pyrite at Mala is comparable to colloform pyrite from the actively forming TAG SMS deposit located at the Mid-Atlantic Ridge (Grant et al. 2018) and from colloform pyrite at the Skouriotissa VMS deposit (Keith et al. 2016a). Primarily, this trace metal enrichment profile reflects the location of colloform pyrite at shallow depths within the VMS mound in close proximity to the seawater interface, and its formation under lower fluid temperatures generated by increased amounts of seawater mixing relative to massive pyrite at deeper stratigraphic levels in the VMS mound (Monecke et al. 2016).

292 Mala colloform pyrite is strongly enriched in Se (Fig. 4) relative to concentrations reported for colloform
293 pyrite at the Skouriotissa VMS deposit (Troodos) that average 12±10 ppm (1σ, n=52; Keith et al. 2016a),
294 black smoker chimneys from Urals VMS deposits that average 9±5 ppm (1σ, n=8; Maslennikov et al. 2009),
295 concentrations of <4.5 ppm at the Semenov vent field (Melekestseva et al. 2014), and the TAG and
296 PACMUS (Roman Ruins) deposits where colloform pyrite did not contain any detectable Se (Wohlgemuth-
297 Ueberwasser et al. 2015; Grant et al. 2018). This concentration is also notably higher than that typically
298 recorded in colloform pyrite in other Troodos VMS deposits where the median concentration is 49 ppm
299 (Martin et al. 2019, 2020). Several studies indicate that Se is preferentially enriched in pyrite that formed
300 in high-temperature regions of the VMS mound or the interior conduit of black smoker chimneys, indicating
301 an affinity for high temperature fluids (Butler and Nesbitt, 1999; Maslennikov et al. 2009; Revan et al.
302 2014; Grant et al. 2018). However, at Mala Se is also enriched in pyrite that is interpreted to have formed
303 at lower temperatures, and we suggest that the enrichment of Se in colloform pyrite is a consequence of an
304 increased magmatic volatile influx.

305 Granular textured massive pyrite occurs towards the margin of the sulfide mound and forms through the
306 collapse and physical reworking of sulfide fragments during the growth of the VMS deposit (Humphris et
307 al. 1995; Petersen et al. 2000). Granular pyrite contains the lowest total measured trace metal content but
308 is relatively enriched in Te compared to other pyrite varieties (Table 1; Fig. 4A). We suggest that metal
309 enrichment profiles in granular pyrite reflect the remobilization and subsequent loss of some metals during
310 zone refining and oxidization of primary massive pyrite at low temperatures (<100°C) at or near the seafloor
311 towards the periphery of the VMS mound (Herzig et al. 1991; Hannington et al. 1998; Fallon et al. 2017;
312 Murton et al. 2019). Assuming that massive pyrite samples represent the primary trace metal content of
313 granular samples prior to reworking, then all elements have been depleted during reworking with the
314 exception of Te. The enrichment of Te, which is readily mobilized under oxidizing and low temperature
315 fluid conditions (e.g., McPhail 1995), possibly indicates that the granular sample analysed was initially
316 enriched in Te prior to reworking.

317 Massive pyrite at Mala occurs as discrete pods throughout the sulfide mound. The trace metal composition
318 is highly variable depending on the individual sample analysed (Table S1 and Fig. S1, ESM). Fluid flow
319 regimes evolve with time in response to permeability fluctuations related to the collapse and occlusion of
320 permeability pathways, leading to the disruption of high-temperature fluid flow pathways within the VMS
321 mound (e.g., Tivey et al. 1995; You and Bickle 1998; Tivey 2007). These local-scale fluctuations (cm to
322 m's) in fluid flow led to changes in temperature and the remobilization of metals stable at low temperatures
323 from areas proximal to zones of high temperature fluid flow (>350°C) within the mound, leading to highly
324 heterogeneous trace metal enrichment profiles between different massive pyrite samples. For example,
325 samples located proximal to high temperature (>350°C) fluid pathways (e.g., MAL 14) are relatively
326 enriched in Se, Co and Te compared with samples that have experienced zone refining during fluid
327 overprinting by later cooler fluids (<350°C) (e.g., MAL 17). Hence, such large variations in trace metal
328 concentrations between massive pyrite samples reflects the dynamic nature of fluid flow within the VMS
329 mound. Alternatively, pyrite that contains low total trace metal concentrations may have been affected by
330 a higher degree of zone refining leading to the localised leaching and remobilization of most trace metals,
331 even those associated with high temperature assemblages as suggested for the Kokkinopezula VMS deposit
332 in Troodos (Hannington et al. 1998). However, high degrees of zone refining are considered to occur in
333 mature VMS deposits, whereas the Mala deposit is suggested to represent an immature system based on the
334 elevated concentration of magmatic volatile elements and low sulfur isotope values (Martin et al. 2021)
335 and, therefore, it is unlikely that enough time has elapsed to reach the high degree of zone refining.

336 Disseminated pyrite occurs as euhedral grains within gypsum (Fig. 2D) and is strongly enriched in Se
337 compared to all other pyrite textures (Fig. 5). This enrichment in Se is most likely a function of the
338 preferential partitioning of Se into disseminated pyrite grains relative to the surrounding gypsum/anhydrite
339 matrix (Yamamoto 1976; Huston et al. 1995). Alternatively, the enrichment of Se could indicate that
340 disseminated pyrite formed under lower fluid temperatures, assuming that Se is transported as H_2Se in the
341 hydrothermal fluid, as thermodynamic models for Se in pyrite predict that it is preferentially enriched at

lower temperatures (150°C) and more oxidizing conditions ($\Sigma SO_4 > \Sigma H_2S$; Huston et al. 1995). However, observations from the active TAG deposit indicate that anhydrite-rich zones, that are analogous to gypsum-rich zones at Mala where disseminated pyrite occurs, typically form at temperatures >350°C (Edmond et al. 1995; Grant et al. 2018; Petersen et al. 2000). Furthermore, pyrite grains appear euhedral with no hematite or magnetite that would indicate more oxidized fluids. Thus, there is no evidence supporting the formation of disseminated pyrite from more oxidized or low-temperature (~150°C) fluids at Mala that are favorable for the incorporation of Se in pyrite (Yamamoto 1976; Huston et al. 1995).

As observed in massive pyrite samples, notable variation exists between individual disseminated samples (Fig. 8). We use the Te and Se content of pyrite as proxies for magmatic volatile influx as these elements are enriched in VMS deposits in volatile-rich subduction influenced environments (Keith et al. 2016b) and Co and As as indicators of high and low temperature fluids, respectively (Grant et al. 2018) (Fig. 8). Samples MAL 18 and MAL 05 are located in the upper mound region, whilst MAL 04 and MAL 11 are located in the lower mound (Fig. 2A). Based on studies of the active TAG mound, spatial trends in the trace metal content of pyrite exists with, for example, Ni, Co and Se enrichment in high-temperature stockwork zones and As, Pb, Zn and Ag enrichment in lower temperature massive pyrite (Grant et al. 2018). Sample MAL 05 contains notably higher Se and Te concentrations relative to all other grains, and is depleted in Co and enriched in As, indicating that it formed at low temperatures. In contrast, sample MAL 18, which also formed in the upper mound area, is relatively depleted in Se, Te and As but is strongly enriched in Co, indicating that it formed from high temperature fluids (>350°C; Metz and Trefry 2000; Keith et al. 2016a; Grant et al. 2018) (Fig. 8). Some samples (e.g., MAL 04) from the lower mound are depleted in As, Co, Te and Se relative to other samples, possibly providing evidence for high degrees of zone refining (Hannington et al. 1998). The trace metal enrichment profile in samples from the lower mound are highly variable with some analyses strongly enriched in Te, Se, Co and As, indicating a change in fluid temperature and/or magmatic volatile influx as the pyrite grain grew. The sporadic variation in trace metal concentrations within individual disseminated pyrite grains indicates the influence of dynamic fluid flow regimes within

the VMS mound that leads to strong and transient physicochemical gradients localised over cm to m scales. Hence, our data indicate that the well-established zone-refining model that is modelled on the active TAG deposit (Humphris et al. 1995; Grant et al. 2018) is more complex when considering the distribution of trace metals, especially when accounting for the distribution of metals over individual mineral grains. This notwithstanding, there are obvious similarities between actively forming SMS deposits and the zonation of metals in black smoker chimneys with the ancient Mala VMS deposit, suggesting that processes that control the mound scale distribution and cycling of trace metals are broadly analogous between the two and did not change since the Cretaceous.

Sulfur isotope systematics

Sulfur isotope analysis of sulfide minerals, such as pyrite, in VMS deposits can be used to discriminate contributions from isotopically-distinct reservoirs of sulfur in hydrothermal fluids, such as sulfur leached from oceanic crust, seawater sulfate, and, SO_2 degassing from shallow magma chambers (Lüders et al. 2001; Hannington et al. 2005; Ono et al. 2007; de Ronde et al. 2011; Keith et al. 2016a; Martin et al. 2020; LaFlamme et al. 2021). The two primary sources of sulfur in Troodos VMS deposits are the bulk Troodos crust that has a sulfur isotope composition of 1 to 0‰ (Alt 1994), Cretaceous seawater sulfate at $\delta^{34}S$ = 18 to 19‰ (Kampschulte and Strauss 2004), and at the Mala VMS deposit, the disproportionation of SO_2 (Martin et al. 2021). The mixing of sulfur sourced from TSR of seawater and the leaching of primary igneous sulfur/sulfide from host rocks (Woodruff and Shanks 1988; Shanks 2001) lead to an average $\delta^{34}S$ value in pyrite of 4.6±2.8‰ (1σ, n=160), indicating that, on average, ~34% of sulfur is sourced from TSR during VMS deposit formation in Troodos (Martin et al. 2020). The Skouriotissa and Sha, and most notably the Mala VMS deposits, contain pyrite with a sulfur isotopic composition that is less than <0‰. Previously, the low $\delta^{34}S$ values in pyrite have been attributed to the disproportion of SO_2 during the degassing of volatiles from a shallow magma chamber (Keith et al. 2016a; Martin et al. 2020). At Mala, disproportionation generates sulfate with a sulfur isotopic composition of 14.5‰ in gypsum (n=26), and pyrite that is depleted in ^{34}S on average by -4.3‰ (n=28) (Martin et al. 2021). Bacterial sulfate reduction

of seawater at low temperatures (<120°C) can also form negative $\delta^{34}S$ values in pyrite as low as -22.2‰ in altered oceanic crust in Troodos, such as those found in pyrite veins in the pillow lavas, indicating that BSR occurred distally to high-temperature VMS deposits in the shallow lava stratigraphy (Alt 1994; Pedersen et al. 2017).

The *in situ* analysis of different pyrite textures indicates that the source of sulfur in the Mala VMS deposit was not constant and evolved with time, leading to variations in $\delta^{34}S$ values across individual pyrite grains. Variation in $\delta^{34}S$ values between pyrite textures relates to mound-scale fluid flow that is directly influenced by the location of specific pyrite samples within the mound that in turn influences pyrite texture (e.g., colloform vs. massive samples). Similar variations are reported across black smoker chimneys where intense gradients in temperature and fluid mixing occur within the chimney wall (Haymon 1983; Crowe and Valley 1992). For example, $\delta^{34}S$ varies from 2.1 to 6.4‰ in pyrite from the interior to exterior chimney wall, respectively, in a black smoker chimney from 1-2°S on the EPR (Meng et al. 2020). Given the large range in $\delta^{34}S$ values of pyrite at Mala, from -17.1‰ to 7.5‰, we suggest four processes that account for the observed variation in the sulfur isotope composition of pyrite: i) TSR of seawater (18 to 19‰), ii) the leaching of igneous sulfide (0 to 1‰), iii) the disproportionation of degassing SO_2 (0 to 1‰) and, iv) BSR.

Firstly, considering variation in sulfur isotope composition with pyrite texture, previous studies note a systematic relationship between stratigraphic depth and $\delta^{34}S$ values in pyrite from the Skouriotissa VMS deposit (Keith et al. 2016a), where enrichment of ^{34}S in shallow euhedral and colloform textured pyrite leads to $\delta^{34}S$ values of 4.7‰ and 4.9‰, respectively (n=4, Keith et al. 2016a). This variation is attributed to the increased proportion of sulfur that is incorporated from TSR of Cretaceous seawater in regions of the VMS mound near the seawater interface. In contrast, deep, stockwork pyrite has a $\delta^{34}S$ value of -1.4‰ indicating lesser amounts of TSR and leaching of igneous sulfur/sulfide and an increased amount of sulfur sourced from the disproportionation of degassing SO_2, producing a sulfur isotope composition in pyrite that is less than the Troodos magmatic mean (0-1‰; Alt 1994) (Keith et al. 2016a). Data presented in this study for the Mala VMS deposit has a range of 24.6‰ (n=31), notably more variable than Skouriotissa with a

range of 7.8‰ (n=29; Keith et al. 2016a; Martin et al. 2020), with no systematic variation between $\delta^{34}S$ values and pyrite texture at Mala (Fig. 6 and 9). Instead, 18 of the 31 analyses across disseminated, granular, colloform and massive textured pyrite contain $\delta^{34}S$ values of less than the Troodos magmatic mean of ~0‰ (Fig. 9; Alt 1994). This supports previous interpretations that have been proposed for the Mala VMS deposit that indicates sulfur was sourced from a mixture of SO_2 disproportion, TSR and leaching of igneous sulfur/sulfide. However, the low $\delta^{34}S$ values measured in massive pyrite (down to -17.1‰), which are much lower than any values previously reported, could be produced either via the low temperature disproportionation of SO_2 or during BSR of Cretaceous seawater. Based on the expected fractionation factors between SO_2 and pyrite (after Sakai 1968), SO_2 disproportion would have had to occur at a temperature of ~120°C to account for the measured depletion in ^{34}S to -17.1‰, assuming a starting SO_2 composition of 0‰. Alternatively, at low temperatures (<120°C) BSR of seawater sulfate can generate large depletions in ^{34}S up to -38.9‰ in pyrite (Habicht and Canfield 1997; Wortmann et al. 2001; Farquhar et al. 2003; Rouxel et al. 2008; Alt and Shanks 2011; Nozaki et al. 2020).

In active seafloor hydrothermal systems evidence for both the low temperature disproportionation of SO_2 and BSR exist. Negative $\delta^{34}S$ values attributed to the disproportion of SO_2 down to -17.5‰ are found in active seafloor hydrothermal systems that experience an increased influx of magmatic volatiles, such as Conical seamount, Papa New Guinea (Gemmell et al. 2004), however typical median values are less extreme, for example the median $\delta^{34}S$ values at Conical seamount are -1.2‰ (n=66) (Petersen et al. 2002; Gemmell et al. 2004) at Hine Hina, Valu Fa Ridge, Lau Basin, -4.5‰ (n=12) (Herzig et al. 1998), at Brothers volcano, Kermadec arc, -2.9‰ (n=87) (Kermadec arc; de Ronde et al. 2005, 2011) and -5.6‰ (n=13) at SuSu Knolls, Manus back-arc basin (Kim et al. 2004), indicating that sulfur was sourced from a combination of SO_2 disproportionation, TSR and leaching of igneous sulfur/sulfide.

Evidence of BSR has also been suggested as an important processes in the Agrokipia B VMS deposit (Troodos) where multiple sulfur isotopes ($\Delta^{33}S$) indicate re-working of sulfide minerals in the upper part of the VMS mound by microbes was an important but localised process (Pedersen et al. 2017). In lower

442 temperature regions of the Troodos stratigraphy, similar $\delta^{34}S$ values of -17.2‰ and as low as -22.2‰ (Alt
443 1994; Pedersen et al. 2017) have been reported for vein pyrite from the upper lava stratigraphy where the
444 occurrence of analcime, natrolite and phillipsite indicate the presence of low temperature fluids (<100°C;
445 Gass and Smewing 1973) where BSR could occur.

446 The negative $\delta^{34}S$ signature, down to -17.1‰, with a median composition of -13.7‰ (n=3) for the massive
447 sulfide sample at Mala, is somewhat enigmatic as both disproportionation of SO_2 and BSR require low fluid
448 temperatures <120°C to explain the observed $\delta^{34}S$ signature. Fractionation factors between SO_2 and pyrite
449 (Sakai, 1968), using an initial value of 0‰, would have had to occur at a temperature of 187°C to explain
450 the median sulfur isotopic composition in pyrite of -13.7‰; assuming that SO_2 disproportionation was the
451 only source of sulfur (i.e. a closed system), which as shown in previous studies is not the case (Ono et al.
452 2007).

453 Combining trace element geochemistry and sulfur isotope data, we suggest that the $\delta^{34}S$ signature is best
454 explained by BSR of seawater. Disproportionation of SO_2 that indicates magmatic volatile influx is, at the
455 mound scale, commonly associated with increased concentrations of Se, Te and Au in the Mala VMS
456 deposit (Martin et al. 2021); however this is not the case in massive pyrite sample MAL 17, that is depleted
457 in Te, Se and Au compared to all other massive pyrite samples. Furthermore, MAL 17 has a median Co
458 concentration of 8.4 ppm (n=10), compared to 38.7 ppm for all massive samples (n=40), further supporting
459 its formation from relatively low temperature fluids (<350°C) (Keith et al. 2016a,b; Monecke et al. 2016;
460 Grant et al. 2018). The relative depletion in Te, Se and Au is not consistent with its formation during
461 magmatic degassing, indicating it most likely formed during the BSR of seawater. This is further supported
462 by the location of the sample on the western margin of the VMS mound (Fig. 2A), and assuming that the
463 mound morphology preserved today is representative of how the Mala VMS deposit formed at the
464 Cretaceous seafloor, the sample is located near the seawater interface where seawater ingress is high and
465 the fluid temperature is expected to be low, possibly <120°C (cf. Pedersen et al. 2017).

466 The sulfur isotopic composition of colloform textured pyrite at Mala has a median $\delta^{34}S$ value of -2.2‰
467 (n=6; Fig. 4). This is significantly lower than the median $\delta^{34}S$ value recorded in colloform pyrite at the
468 Skouriotissa VMS deposit of 4.9‰ (n=2; Keith et al. 2016a), the Ice VMS deposit (Yukon, Canada) at
469 5.0‰ (n=8; McDonald et al. 2018), and the Ezuri VMS deposit (Hokuroko, Japan) at 4.5‰ (n=16; Barrie
470 et al. 2009). The positive values found in colloform pyrite in most VMS deposits demonstrate that the
471 primary source of sulfur is the leaching of igneous basement and TSR of seawater (Ohmoto 1996; Barrie
472 et al. 2009; Keith et al. 2016a; McDonald et al. 2018). By contrast, $\delta^{34}S$ values in colloform pyrite at Mala
473 are less than the Troodos magmatic mean (0-1‰; Alt 1994) indicating that sulfur was not *only* sourced via
474 TSR of Cretaceous seawater and the leaching of igneous lithologies, instead indicating that colloform pyrite
475 formed during the disproportionation of SO_2. Using the fractionation between SO_2 and pyrite (Sakai 1968),
476 the expected fractionation at 350°C would be 8.6‰. In order to explain the observed fractionation between
477 the median $\delta^{34}S$ value in colloform pyrite (2.2‰) and primary igneous sulfur/sulfide (0‰) the fluid
478 temperature would have had to be >880°C. As previously established for bulk rock samples, this
479 temperature is unrealistically high for VMS deposit formation, hence we suggest that the disproportion of
480 SO_2 occurred at lower fluid temperatures where fractionation between SO_2 and pyrite is greater and that the
481 higher than anticipated $\delta^{34}S$ values in colloform pyrite reflects the addition of a ^{34}S enriched source from
482 both TSR and the leaching of igneous sulfur/sulfide providing an additional source of sulfur in colloform
483 pyrite.

484 Disseminated pyrite grains exhibit the largest variation in $\delta^{34}S$ values with a median of 0.7‰ and a range
485 of 16.8‰ (n=14). To assess if the pyrite analysed are singular grains or aggregates of sub-grains, etching
486 was used to reveal any internal variation (Fig. 7). Sample MAL 05 (Fig. 7A) exhibits internal variation
487 appearing as three different colored sections, indicating it is formed from three sub-grains. In contrast, the
488 etched surface of MAL 11A and B does not show any notable variation indicating that they are a single
489 continuous grain (Fig. 7B and C).

The sulfur isotopic composition of individual pyrite grains is highly variable across disseminated pyrite grains with $\delta^{34}S$ values ranging from -10.9‰ to 2.5‰ (within a single sub-grain), suggesting that the source of sulfur changed as the pyrite crystal grew. However, there is no systematic variation in sulfur isotope composition between the core and rim of the grain (Fig. 7A), and the two analyses located at the margin of the grain yield $\delta^{34}S$ values of 2.5‰ and -10.9‰, respectively. Instead, $\delta^{34}S$ values appear to gradually decrease across the pyrite grain indicating a change in the source of sulfur as the grain grew (Fig. 7A). In other pyrite grains a more systematic pattern is discernable where the rim of the grain is enriched in ^{34}S relative to the core (Fig. 7B and C). This variation could be related to either pulsed fluid flow events (Butterfield et al. 1994, 2011; Jamieson et al. 2013) that generate fluctuations in fluid flux, temperature, and the chemical and physical (e.g., phase separation) composition of hydrothermal fluids (Lalou et al. 1990, 1998; Butterfield et al. 1994) or local scale variation in mound-scale fluid flow in response to the collapse and occlusion of permeability pathways during growth of the VMS mound (Klienrock and Humphris 1996; Humphris et al. 1995; Hannington et al. 1998; Petersen et al. 2000).

Pulsed fluid flow events are linked to magmatic intrusions at depth within the oceanic crust that provide a renewed source of heat that increases the temperature of venting hydrothermal fluid, volatile influx (e.g., H_2S and SO_2), and the metal content of fluid vented at the seafloor (Von Damm 1990; Von Damm et al. 1995; Butterfield et al. 1997; Andersen et al. 2017). Several studies document temporal variations in total sulfur concentrations and major anions (e.g., Cl^-) in hydrothermal vent fluids sampled from active vent sites demonstrating that the flux of sulfur in VMS deposits varies temporally (Butterfield and Massoth, 1994; Von Damm et al. 1995; Butterfield et al. 1997, 2011; Von Damm 1995). It does however remain enigmatic exactly what these variations mean, for example variations in fluid H_2S concentration could also be produced during the precipitation or dissolution of sulfide minerals below the seafloor (Reed and Palandri 2006) or during the segregation of H_2S into a vapor phase, thus linking these variations to magmatic intrusion events is challenging (Von Damm et al. 1995; Butterfield et al. 1997). The dating of SMS deposits ($^{210}Pb/Pb$, $^{230}Th/^{234}U$ and ^{14}C) also provides evidence of aperiodic fluid flow with apparent pulses of activity recorded at the active TAG mound every 2,000 to 6,000 years (Lalou et al. 1993; You and Bickle1998).

In Troodos VMS deposits there are no hydrothermal fluids left to sample nor are the deposits young enough to be dated using radiometric isotope techniques commonly applied to active SMS deposits, however variation in rare earth element profiles and Sr isotopes ($^{87}Sr/^{86}Sr$) in epidote from the sheeted dykes complex and plagiogranites, that formed during hydrothermal alteration of the oceanic crust indicate the episodic release of volatiles into the Troodos hydrothermal systems (Fox et al. 2020). If this was the case then evidence of pulsed magmatic influx may have been recorded on the scale of individual pyrite mineral grains as variations in across grain sulfur isotope composition (Fig. 7). Following a volcanic event or the liberation of magmatic volatiles from the roof of an underlying magma chamber during dyking events, as hypothesized for Troodos (Gillis and Roberts 1999; Fox et al. 2020), the disproportionation of SO_2 occurs and progressively decreases with time from the event, reducing the flux of SO_2 and subsequent disproportionation in the overlying hydrothermal system, and the primary source of sulfur changes from one strongly influenced by disproportionation of SO_2 to one dominated by TSR and leaching of igneous sulfur/sulfide. This would produce a pronounced shift in the sulfur isotopic composition across individual pyrite grains from negative $\delta^{34}S$ values indicating SO_2 disproportionation to values >0‰ that indicate increasing amounts of sulfur sourced from TSR and the leaching of igneous sulfur/sulfide (e.g., Fig. 7C). A similar model has been proposed by earlier studies to explain the sporadic preservation of $\delta^{34}S$ values down to -5.5‰ in the Sha VMS deposit (Martin et al. 2020). The zonation and aperiodic nature of these fluctuations in sulfur isotope composition across each mineral grain may be linked to the pulsed nature of fluid flow during VMS deposit formation, however, further high-resolution mineral-scale data including mapping of individual mineral grains is required to ascertain the true significance and validity of mineral-scale sulfur isotope data when applied to system scale pulsed ore-forming processes.

A comparison between bulk and *in situ* sulfur isotope data

The sulfur isotope composition of pyrite from the Mala VMS deposit has previously been assessed using bulk analytical methods on powdered wholerock samples or pure mineral concentrates (Fig. 9). Using bulk analytical methods, the $\delta^{34}S$ values in pyrite range from -7.6‰ to 0.1‰ with a median value of -4.3‰

(n=28; Martin et al. 2021) (Fig. 9). Using *in situ* sulfur isotope data collected on the same samples, the sulfur isotope composition of pyrite varies from -17.1‰ to 7.5‰ with a median value of -1.0‰ (n=31); variation larger than for the same samples using bulk analytical techniques (Fig. 9). When comparing between whole rock and *in situ* datasets, on average the difference between the same sample analysed by SIMS and wholerock methods was 4.9‰ (n=6 samples), with some samples, such as MAL 17, exhibiting a difference of 7.3‰ between methods. This difference between analytical scales indicates that a significant amount of variability, and therefore changes in sulfur source and by implication metal source are being overlooked when using bulk analytical methods compared to *in situ* mineral-scale data. This trend is comparable to those recognized at Axial Seamount where the bulk analysis of pyrite yield a range of 1.1 to 3.9‰ (Hannington and Scott 1988) whilst *in situ* analysis exhibits more variability with a range of 1.2 to 6.9‰ (Crowe and Valley 1992) or at 1-2° N on the East Pacific Rise (EPR) where bulk pyrite analyses have a range of 3.0 to 5.8‰ (Zeng et al. 2017) versus *in situ* analysis of pyrite that ranges from 1.8 to 7.5‰ (Meng et al. 2019).

To illustrate the disparity between analytical scales we highlight two examples of analytical transects across pyrite grains (n=23 spots, Fig. 10A). Across a coarse-grained (~1 cm) pyrite grain with three sub-grains that occurs within gypsum $\delta^{34}S$ values exhibit the largest intra-sample range from -10.9‰ to 4.9‰ with a median of 2.0‰ (n=7) (Fig. 10A). Bulk analysis of the same sample yielded $\delta^{34}S$ values of -0.5‰ and -1.2‰ (Martin et al. 2021). The application of *in situ* analytical methods indicates a variable source of sulfur with values of -10.9‰ indicating dominantly SO_2 disproportionation and values of 4.5‰ signifying a larger contribution of sulfur sourced via TSR of seawater and the leaching of igneous sulfur/sulfide (Fig. 9). A similar difference between analytical methods is evident in all other samples we analysed (Table S3, ESM); demonstrating that data obtained at different analytical scales (i.e. mineral vs. bulk samples) can change the resulting interpretation that is reached.

Can magmatic volatile influx be traced at the mineral-scale?

Previous studies have identified an enrichment of Te, Se, Au, Bi, As, Sb, Pb and Hg in SMS deposits that form in subduction influenced environments relative to MOR hosted hydrothermal systems, indicating a link between metal enrichment and magmatic volatile degassing (Hannington et al. 1999; de Ronde et al. 2011; Berkenbosch et al. 2012; Layton-Matthews et al. 2013; Wohlgemuth-Ueberwasser et al. 2015; Fuchs et al. 2019; Martin et al. 2019; Mathieu 2019; Patten et al. 2020). For example, at the Brothers NW Caldera site (Kermadec arc), a positive correlation exists between decreasing $\delta^{34}S$ values (to -4.6‰ in sphalerite) and Au concentration, indicating a link between magmatic volatile influx and Au enrichment (de Ronde et al. 2011). If certain metals were sourced from a magmatic volatile phase in the Mala VMS deposit, then they would be expected to show increased concentrations at low $\delta^{34}S$ values that indicate an increased magmatic volatile influx associated with SO_2 disproportionation (e.g., Herzig et al. 1998). As previously established, sulfur isotopic ratios exhibit notable variation across individual pyrite grains indicating a variation in sulfur source that we ultimately relate to a variable magmatic volatile influx. If magmatic volatile influx occurred as aperiodic releases from the plagiogranites in Troodos into the overlying hydrothermal systems, a coupled relationship between sulfur isotopes and the enrichment of trace metals that are associated with increased levels of volatile influx (e.g., Te and Se) should exist in pyrite (Fox et al. 2020). However, our data exhibits limited correlation between Te, Se, Au, As and Co and $\delta^{34}S$ values indicating that the primary magmatic signature/zonation in trace metals, if initially present, was rapidly modified within the VMS mound.

Selenium has been widely applied as an indicator of magmatic volatile influx with Se/S ratios in pyrite used as evidence of an increased magmatic volatile influx in VMS deposits (Yamamoto 1976; Huston et al. 1995; Hannington et al. 1999; Layton-Matthews et al. 2008, 2013; Martin et al. 2019). The contribution of Se from a magmatic volatile phase at Mala is largely supported at the deposit scale by negative $\delta^{34}S$ values in pyrite and a moderate positive correlation between Te and Se (R^2=0.67); a trend that is not observed in any

588 other Troodos VMS deposit (Martin et al. 2021). However, mineral grain scale observations show that a
589 more complex relationship exists (Fig. 10 and 11).

590 If the Se content of pyrite is a reliable proxy for magmatic volatile influx at Mala, then a negative correlation
591 is expected between Se content and $\delta^{34}S$ values in pyrite, with high Se contents occurring in the samples
592 with low $\delta^{34}S$ values indicating a coupled relationship (Yamamoto 1976). The Se content of sample MAL
593 05, a disseminated pyrite grain in gypsum (Fig. 10A) ranges from 839 to 1727 ppm with the highest Se
594 concentration corresponding to a $\delta^{34}S$ value of 2.5‰. The two lowest Se concentrations of 839 and 1273
595 ppm correspond to the highest $\delta^{34}S$ values measured in MAL 05 of 4.9 and 5.9‰, respectively (Fig. 10A).
596 However, the two lowest $\delta^{34}S$ values of -2.0 and -10.9‰ do not correspond to the highest Se content. Thus,
597 Se content does not accurately track magmatic volatile influx, if this were the case then a strong correlation
598 between $\delta^{34}S$ values and Se concentration would occur, however this is not observed (Fig. 11B).

599 Renewed volatile influx is driven by magmatic intrusions at depth below the seafloor that lead to an increase
600 in fluid temperatures preceding the intrusive event, for example at 9° 46.5' N on the East Pacific Rise where
601 vent fluid temperature varied from 403°C directly after the intrusive event to 322°C three years later (Von
602 Damm et al. 1995). High Co concentrations in pyrite have been suggested to indicate elevated fluid
603 temperatures (>350°C), therefore Co should be enriched at low $\delta^{34}S$ values that precede the intrusive event
604 (Butterfield et al. 1997; Keith et al. 2016a,b; Grant et al. 2018). Arsenic is expected to exhibit the inverse
605 trend as it is concentrated in low temperature pyrite (<350°C) and is expected to be enriched at high $\delta^{34}S$
606 values representing periods of low magmatic volatile influx and correspondingly cooler fluids (Monecke et
607 al. 2016; Grant et al. 2018). Thus, systematic shifts in Te and Se, that indicate renewed volatile influx, and
608 As and Co that signify changes in fluid temperature should correlate with changes in $\delta^{34}S$ values in pyrite
609 if they are reliable tracers of magmatic volatile influx at the mineral-scale; we assess this relationship in
610 disseminated pyrite grains at Mala.

611 In sample MAL 05 Co concentration varies from 12 to 23 ppm (Fig. 10A), exhibiting only a minor
612 correlation (R^2=0.3) with $\delta^{34}S$ values (Fig. 10A). Arsenic concentrations are more variable than Co ranging

613 from 5 to 145 ppm with the highest concentration corresponding to a $\delta^{34}S$ value of -2.0‰, but with no
614 notable correlation between As and $\delta^{34}S$ values (R^2 =0.02). A similar trend is evident for Te data with an
615 R^2 value of 0.1 (Fig.10 and 11).

616 In other disseminated grains (Fig. 10B; MAL 11A) the highest Se and Co content correspond to the lowest
617 $\delta^{34}S$ value of 0.2‰, whilst Te exhibits the inverse trend (Fig. 10B). A similar trend is also discernable in
618 MAL 11B where the sulfur isotope composition of pyrite exhibits a saw tooth pattern ranging from -2.5‰
619 to 0.4‰ (Fig. 10C). Selenium and Te concentrations exhibit a moderate correlation with $\delta^{34}S$ values with
620 an R^2 value of 0.6 and 0.3, respectively. Thus, no clear relationship exists between trace metals and sulfur
621 isotope composition across disseminated pyrite grains at Mala.

622 For all other samples considered in this study, our data indicate that there is no notable correlation between
623 Te, Se and Co with $\delta^{34}S$ values in individual pyrite grains or within the different textures analysed (Fig.
624 11). The highest measured Se concentration of 3261 ppm corresponds to a $\delta^{34}S$ value of 0‰, whilst lower
625 values of -2.5‰ within the same mineral grain, which suggest an increased magmatic volatile influx
626 correspond to a Se concentration of 325 ppm (Fig. 11A). We exclude massive pyrite sample MAL 17 from
627 our interpretation that is influenced by BSR of seawater leading to a low $\delta^{34}S$ value in pyrite and notably
628 lower concentrations of Se, Te and Co relative to massive and disseminated samples (Fig. 11).

629 Our investigation indicates that variations in Te, Se, Co and As concentrations at the mineral-scale cannot
630 be linked to variations in magmatic volatile influx at the Mala VMS deposit (Fig. 12). The lack of
631 correlation between $\delta^{34}S$ values and Te, Se, Co and As in the Mala VMS deposit probably reflects the
632 localized remobilization of trace elements during zone refining related to fluctuations in mound scale fluid
633 flow related to the collapse and occlusion of fluid pathways during the growth of the mound that leads to
634 localised zone refining of trace metals in pyrite (Fig. 12). Any initial zonation of trace metals in pyrite
635 related to the influx of magmatic volatiles is overprinted by later fluid flow that led to the mobilization of
636 trace metals but does not alter the original sulfur isotope composition of <0‰ related to magmatic volatile
637 influx and SO_2 disproportionation, hence, this explains the lack of correlation between $\delta^{34}S$ values and Te,

638 Se, Co and As at the mineral-scale at Mala (Fig. 12). To investigate this process, further high-resolution *in*
639 *situ* isotopic and trace element geochemistry and information on the diffusion rates of trace metals and
640 sulfur in pyrite (e.g., Cherniak 2010) is needed to understand chemical zonation at the scale of individual
641 mineral grains.

642 Summary and conclusion

643 The distribution of trace metals between different pyrite textures in the Mala VMS deposit appears broadly
644 analogous to actively forming mafic SMS deposits. Colloform pyrite that formed near the seawater interface
645 is enriched in low temperature elements such as As and Au relative to massive samples that contain euhedral
646 pyrite that are relatively enriched in high temperature metals Se, Co and Te. Granular samples that formed
647 during the reworking of massive pyrite are depleted in all metals (except Te) due to the mobilization and
648 leaching of metals during low temperature fluid flow at the margin of the VMS mound. There is no
649 systematic variation in trace metal enrichment profiles with depth in the VMS mound, instead variation
650 between individual samples can be attributed to dynamic fluid flow patterns within the VMS mound and
651 the localised (cm to m scale) zone refining of metals around individual fluid conduits that vary spatially
652 and temporally during mound growth (Fig. 12). All pyrite textures appear to be enriched in Se relative to
653 both Troodos VMS deposits and mafic hosted VMS deposits more widely indicating a Se-rich magmatic
654 volatile dominated source.

655 The large range in the $\delta^{34}S$ composition of pyrite relative to previous studies and mafic VMS deposits more
656 widely can be explained by varying combinations of four main processes: i) TSR, ii) leaching of
657 sulfur/sulfide from host rocks, iii) SO_2 disproportionation and iv) BSR. Thermochemical sulfate reduction
658 of seawater and the leaching of igneous sulfur/sulfide generates $\delta^{34}S$ values in pyrite that are higher than
659 the Troodos magmatic mean of 0-1‰, whilst low values that are less than this are produced during the
660 addition of sulfur from the disproportionation of SO_2 during the degassing of shallow magma chambers.

When combined with trace element geochemistry, we suggest low $\delta^{34}S$ values (to -17.1‰) formed during the BSR of seawater in the upper VMS mound at temperatures of <120°C.

Mineral-scale sulfur isotope data exhibits notably more variation than the same samples analysed via bulk rock analytical methods. We observe greater amounts of variation over a single pyrite grain than recorded across all bulk rock analyses with $\delta^{34}S$ values ranging from -10.9 to 2.5‰. Analytical transects across individual mineral grains indicate that the source of sulfur in the Mala VMS deposit was variable and alternated between disproportionation of SO_2, TSR and the leaching of igneous sulfur/sulfide as the pyrite grain grew. Such variation is not evident when using bulk analytical techniques for sulfur isotopes and warrants further detailed investigation.

Linking variations in trace metal enrichment profiles and sulfur isotopes is key in understanding the role of magmatic volatiles as a potential metal source in mafic VMS deposits. However, findings of this study indicate no simple correlation between magmatic volatile elements such as Te and Se and $\delta^{34}S$ values. We attribute this decoupled relationship to local scale fluid flow within the mound that leads to the remobilization of trace metals during zone refining. Pyrite retains $\delta^{34}S$ values that indicate disproportionation (<0‰) but can be depleted in magmatic volatile metals.

Acknowledgements

The authors acknowledge the support of the Geological Survey Department of Cyprus, especially Costas Costantinou and Andreas Zissimos. We thank Michael Green and Ifigenia Gavriel for discussion and assistance in the field. This research was partly funded by the NERC SoS consortium grant NE/M010848/1 “TeaSe: tellurium and selenium cycling and supply” awarded to Cardiff University and by the Canadian Research Chair program awarded to John W. Jamieson. We thank Stefanie Brueckner and associate editor Mostafa Fayek for their constructive reviews and editor-in-chief Georges Beaudoin for the editorial handling of this manuscript.

References

Adamides NG (2010) Mafic-dominated volcanogenic sulphide deposits in the Troodos ophiolite, Cyprus Part 2 – A review of genetic models and guides for exploration. Appl Earth Sci 119:193–204

Alt JC (1994) A sulfur isotopic profile through the Troodos ophiolite, Cyprus: Primary composition and the effects of seawater hydrothermal alteration. Geochim Cosmochim Acta 58:1825–1840

Alt JC, Shanks WC (2011) Microbial sulfate reduction and the sulfur budget for a complete section of altered oceanic basalts, IODP Hole 1256D (eastern Pacific). Earth Planet Sci Lett 310:73–83

Andersen C, Theissen-Krah S, Hannington M, Rüpke L, Petersen S (2017) Faulting and off-axis submarine massive sulfide accumulation at slow spreading mid-ocean ridges: A numerical modeling perspective. Geochem Geophys Geosystems 18:2305–2320

Banerjee NR, Gillis KM, Muehlenbachs K (2000) Discovery of epidosites in a modern oceanic setting, the Tonga forearc. Geology 28:151-154

Barrie CD, Boyce AJ, Boyle AP, Williams PJ, Blake K, Ogawara T, Akai J, Prior DJ (2009) Growth controls in colloform pyrite. Am Mineral. 94:415–42

Berkenbosch HA, de Ronde CEJ, Gemmell JB, McNeill AW, Goemann K (2012) Mineralogy and Formation of Black Smoker Chimneys from Brothers Submarine Volcano, Kermadec Arc. Econ Geol 107:1613–1633

Brazilian Metals Group (2013) High-Grade Copper-Zinc Sulphide Mineralisation Identified At Mala Prospect – Vrechia. www.bmgl.com.au/investors/annual-reports. Accessed 30 July 2018

Brueckner SM, Piercey SJ, Layne GD, Piercey G, Sylvester PJ, (2015) Variations of sulphur isotope signatures in sulphides from the metamorphosed Ming Cu(−Au) volcanogenic massive sulphide deposit, Newfoundland Appalachians, Canada. Miner Deposita 50:619–640

Butler IB, Nesbitt RW (1999) Trace element distributions in the chalcopyrite wall of a black smoker chimney: insights from laser ablation inductively coupled plasma mass spectrometry (LA–ICP–MS). Earth Planet Sci Lett 167:335–345

709 Butterfield DA, Massoth GJ (1994) Geochemistry of north Cleft segment vent fluids: Temporal changes
710 in chlorinity and their possible relation to recent volcanism. J Geophys Res Solid Earth 99:4951–
711 4968
712 Butterfield DA, McDuff RE, Mottl MJ, Lilley MD, Lupton JE, Massoth GJ (1994) Gradients in the
713 composition of hydrothermal fluids from the Endeavour segment vent field: Phase separation and
714 brine loss. J Geophys Res Solid Earth 99:9561–9583
715 Butterfield DA, Nakamura K, Takano B, Lilley MD, Lupton JE, Resing JA, Roe KK (2011) High SO2
716 flux, sulfur accumulation, and gas fractionation at an erupting submarine volcano. Geology 39:
717 803–806
718 Cherniak, DJ (2010) Diffusion in Carbonates, Fluorite, Sulfide Minerals, and Diamond. Rev Mineral
719 Geochem 72:871–897
720 Cook NJ, Ciobanu CL, Mao J (2009) Textural control on gold distribution in As-free pyrite from the
721 Dongping, Huangtuliang and Hougou gold deposits, North China Craton (Hebei Province,
722 China). Chem Geol 264:101–121
723 de Ronde CEJ, Massoth GJ, Butterfield DA, Christenson BW, Ishibashi J, Ditchburn RG, Hannington
724 MD, Brathwaite RL, Lupton JE, Kamenetsky VS, Graham IJ, Zellmer GF, Dziak RP, Embley
725 RW, Dekov VM, Munnik F, Lahr J, Evans LJ, Takai K, (2011) Submarine hydrothermal activity
726 and gold-rich mineralization at Brothers Volcano, Kermadec Arc, New Zealand. Miner Deposita
727 46:541–584
728 de Ronde CEJ, Hannington MD, Stoffers P, Wright IC, Ditchburn RG, Reyes AG, Baker ET, Massoth
729 GJ, Lupton JE, Walker SL, Greene RR, Soong CWR, Ishibashi J, Lebon GT, Bray CJ, Resing JA,
730 (2005) Evolution of a Submarine Magmatic-Hydrothermal System: Brothers Volcano, Southern
731 Kermadec Arc, New Zealand. Econ Geol 100:1097–1133
732 Edmond JM, Campbell AC, Palmer MR, Klinkhammer GP, German CR, Edmonds HN, Elderfield H,
733 Thompson G, Rona P (1995) Time series studies of vent fluids from the TAG and MARK sites

(1986, 1990) Mid-Atlantic Ridge: a new solution chemistry model and a mechanism for Cu/Zn zonation in massive sulphide orebodies. Geol Soc Lond Spec Publ 87:77–86

Eldridge CW, Barton PB, and Ohmoto H (1983) Mineral textures and their bearing on formation of the Kuroko orebodies. Econ Geol Mono 5: 241–281

Fallon EK, Petersen S, Brooker RA, Scott TB (2017) Oxidative dissolution of hydrothermal mixed-sulphide ore: An assessment of current knowledge in relation to seafloor massive sulphide mining. Ore Geol Rev 86:309–337

Farquhar J, Johnston DT, Wing BA, Habicht KS, Canfield DE, Airieau S, Thiemens MH (2003) Multiple sulphur isotopic interpretations of biosynthetic pathways: implications for biological signatures in the sulphur isotope record. Geobiology 1:27–36

Fox S, Katzir Y, Bach W, Schlicht L, Glessner J (2020) Magmatic volatiles episodically flush oceanic hydrothermal systems as recorded by zoned epidote. Commun Earth Environ 1:52

Fuchs S, Hannington MD, Petersen S (2019) Divining gold in seafloor polymetallic massive sulfide systems. Miner Deposita 54:789–820

Galley AG, Hannington MD, Jonasson IR (2007). Volcanogenic massive sulphide deposits, in: Mineral Deposits of Canada: A Synthesis of Major Deposit Types. Geological Association of Canada, St. John's, Newfoundland, pp.141–162

Gass IG (1968) Is the Troodos Massif of Cyprus a Fragment of Mesozoic Ocean Floor? Nature 220:39–42

Gass IG, Smewing JD, (1973) Intrusion, Extrusion and Metamorphism at Constructive Margins: Evidence from the Troodos Massif, Cyprus. Nature 242:26–29

Gemmel JB, Sharpe R, Jonasson IR, Herzig PM (2004) Sulfur Isotope Evidence for Magmatic Contributions to Submarine and Subaerial Gold Mineralization: Conical Seamount and the Ladolam Gold Deposit, Papua New Guinea. Econ Geol 99:1711–1725

758 Genna D, Gaboury D (2015) Deciphering the Hydrothermal Evolution of a VMS System by LA-ICP-MS
759 Using Trace Elements in Pyrite: An Example from the Bracemac-McLeod Deposits, Abitibi,
760 Canada, and Implications for Exploration. Econ Geol 110:2087–2108
761 Gillis KM, Roberts MD (1999) Cracking at the magma–hydrothermal transition: evidence from the
762 Troodos Ophiolite, Cyprus. Earth Planet Sci Lett 169:227–244
763 Grant HLJ, Hannington MD, Petersen S, Frische M, Fuchs SH (2018) Constraints on the behavior of trace
764 elements in the actively-forming TAG deposit, Mid-Atlantic Ridge, based on LA-ICP-MS
765 analyses of pyrite. Chem Geol 498:45–71
766 Habicht KS, Canfield DE (1997) Sulfur isotope fractionation during bacterial sulfate reduction in organic-
767 rich sediments. Geochim Cosmochim Acta 61:5351–5361
768 Halbach P, Blum N, Münch U, Plüger W, Garbe-Schönberg D, Zimmer M (1998) Formation and decay of
769 a modern massive sulfide deposit in the Indian Ocean. Miner Deposita 33:302–309
770 Hannington MD, Bleeker W, Kjarsgaard I (1999) Sulfide Mineralogy, Geochemistry, and Ore Genesis of
771 the Kidd Creek Deposit: Part II. The Bornite Zone*, in: Hannington, MD, Barrie CT (ed), The
772 Giant Kidd Creek Volcanogenic Massive Sulfide Deposit, Western Abitibi Subprovince, Canada.
773 Society of Economic Geologists, Littleton Colorado
774 Hannington MD, de Ronde CEJ, Petersen S (2005) Sea-floor tectonics and submarine hydrothermal
775 systems, in: Hedenquist JW, Thompson JFH, Goldfarb RJ, Richards JP (ed.), Economic Geology
776 100th Anniversary Volume. Society of Economic Geologists, Littelton, Colorado, USA, pp. 111–
777 141
778 Hannington MD, Galley AG, Herzig PM, Petersen S (1998) Comparison of the TAG mound and
779 stockwork complex with Cyprus-type massive sulfide deposits. In: Herzig, P.M., Humphris, S.E.,
780 Miller, D.J., and Zierenberg, R.A. (ed), 1998 Proceedings of the Ocean Drilling Program,
781 Scientific Results, Vol. 158

Herzig PM, Hannington MD, Arribas Jr. A (1998) Sulfur isotopic composition of hydrothermal precipitates from the Lau back-arc: implications for magmatic contributions to seafloor hydrothermal systems. Miner Deposita 33:226–237

Herzig PM, Hannington MD, Scott SD, Maliotis G, Rona PA, Thompson G (1991) Gold-rich sea-floor gossans in the Troodos Ophiolite and on the Mid-Atlantic Ridge. Econ Geol 86:1747–1755

Humphris SE, Herzig PM, Miller DJ, Alt JC, Becker K, Brown D, Brügmann G, Chiba H, Fouquet Y, Gemmell JB, Guerin G, Hannington MD, Holm NG, Honnorez JJ, Iturrino GJ, Knott R, Ludwig R, Nakamura K, Petersen S, Reysenbach A-L, Rona PA, Smith S, Sturz AA, Tivey MK, Zhao X, (1995) The internal structure of an active sea-floor massive sulphide deposit. Nature 377:713–716

Huston DL, Relvas JMRS, Gemmell JB, Drieberg S (2011) The role of granites in volcanic-hosted massive sulphide ore-forming systems: an assessment of magmatic–hydrothermal contributions. Miner Deposita 46:473–507

Huston DL, Sie SH, Suter GF (1995) Selenium and its importance to the study of ore genesis: the theoretical basis and its application to volcanic-hosted massive sulfide deposits using pixeprobe analysis. Nucl. Instrum. Methods Phys Res Sect B Beam Interact Mater At, Nuclear Microprobe Technology and Applications 104:476–480

Jamieson JW, Hannington MD, Clague DA, Kelley DS, Delaney JR, Holden JF, Tivey MK, Kimpe LE, (2013) Sulfide geochronology along the Endeavour Segment of the Juan de Fuca Ridge. Geochem Geophys Geosystems 14:2084–2099

Jowitt SM, Jenkin GRT, Coogan LA, Naden J (2012). Quantifying the release of base metals from source rocks for volcanogenic massive sulfide deposits: Effects of protolith composition and alteration mineralogy. J Geochem Explor 118:47–59

Kampschulte A, Strauss H (2004) The sulfur isotopic evolution of Phanerozoic seawater based on the analysis of structurally substituted sulfate in carbonates. Chem Geol 204:255–286

806 Keith M, Haase KM, Klemd R, Krumm S, Strauss H (2016a) Systematic variations of trace element and
807 sulfur isotope compositions in pyrite with stratigraphic depth in the Skouriotissa volcanic-hosted
808 massive sulfide deposit, Troodos ophiolite, Cyprus. Chem Geol 423:7–18
809 Keith M, Haase KM, Klemd R, Smith DJ, Schwarz-Schampera U, Bach W (2018) Constraints on the
810 source of Cu in a submarine magmatic-hydrothermal system, Brothers volcano, Kermadec island
811 arc. Contrib Mineral Petrol 173:40
812 Keith M, Häckel F, Haase KM, Schwarz-Schampera U, Klemd R, (2016b) Trace element systematics of
813 pyrite from submarine hydrothermal vents. Ore Geol Rev 72:728–745
814 Kim J, Lee I, Lee K-Y (2004) S, Sr, and Pb isotopic systematics of hydrothermal chimney precipitates
815 from the Eastern Manus Basin, western Pacific: Evaluation of magmatic contribution to
816 hydrothermal system. J Geophys Res Solid Earth 109
817 Kleinrock MC, Humphris SE (1996) Structural control on sea-floor hydrothermal activity at the TAG
818 active mound. Nature 382:149–153
819 Kusakabe M, Komoda Y, Takano B, Abiko T (2000) Sulfur isotopic effects in the disproportionation
820 reaction of sulfur dioxide in hydrothermal fluids: implications for the δ34S variations of dissolved
821 bisulfate and elemental sulfur from active crater lakes. J Volcanol Geotherm Res 97:287–307
822 LaFlamme C, Barré G, Fiorentini ML, Beaudoin G, Occhipinti S, Bell J (2021) A significant seawater
823 sulfate reservoir at 2.0 Ga determined from multiple sulfur isotope analyses of the
824 Paleoproterozoic Degrussa Cu-Au volcanogenic massive sulfide deposit, Western Australia.
825 Geochim Cosmochim Acta 295:178–193
826 Lalou C, Münch U, Halbach P, Reyss J-L (1998) Radiochronological investigation of hydrothermal
827 deposits from the MESO zone, Central Indian Ridge. Mar Geol 149:243–254
828 Lalou C, Reyss J-L, Brichet E, Arnold M, Thompson G, Fouquet Y, Rona PA (1993) New age data for
829 Mid-Atlantic Ridge hydrothermal sites: TAG and Snakepit chronology revisited. J Geophys Res
830 98:9705–9713

831 Lalou C, Thompson G, Arnold M, Brichet E, Druffel E, Rona PA (1990) Geochronology of TAG and
832 Snakepit hydrothermal fields, Mid-Atlantic Ridge: witness to a long, complex hydrothermal
833 history. Earth Planet Sci Lett 97:113-128

834 Layton-Matthews D, Leybourne MI, Peter JM, Scott SD, Cousens B, Eglington BM (2013) Multiple
835 sources of selenium in ancient seafloor hydrothermal systems: Compositional and Se, S, and Pb
836 isotopic evidence from volcanic-hosted and volcanic-sediment-hosted massive sulfide deposits of
837 the Finlayson Lake District, Yukon, Canada. Geochim Cosmochim Acta 117:313–331

838 Layton-Matthews D, Peter JM, Scott SD, Leybourne MI (2008) Distribution, Mineralogy, and
839 Geochemistry of Selenium in Felsic Volcanic-Hosted Massive Sulfide Deposits of the Finlayson
840 Lake District, Yukon Territory, Canada. Econ Geol 103:61–88

841 Lode S, Piercey SJ, Layne GD, Piercey G, Cloutier J (2017) Multiple sulphur and lead sources recorded
842 in hydrothermal exhalites associated with the Lemarchant volcanogenic massive sulphide deposit,
843 central Newfoundland, Canada. Miner Deposita 52:105-128

844 Lüders V, Pracejus B, Halbach P (2001) Fluid inclusion and sulfur isotope studies in probable modern
845 analogue Kuroko-type ores from the JADE hydrothermal field (Central Okinawa Trough, Japan).
846 Chem Geol 173:45–58

847 Martin AJ, Keith M, McDonald I, Haase KM, McFall KA, Klemd R, MacLeod CJ (2019) Trace element
848 systematics and ore-forming processes in mafic VMS deposits: Evidence from the Troodos
849 ophiolite, Cyprus. Ore Geol Rev 106:205–225

850 Martin AJ, Keith M, Parvaz DB, McDonald I, Boyce AJ, McFall KA, Jenkin GRT, Strauss H, MacLeod
851 CJ (2020) Effects of magmatic volatile influx in mafic VMS hydrothermal systems: Evidence
852 from the Troodos ophiolite, Cyprus. Chem Geol 531:119325

853 Martin AJ, McDonald I, MacLeod CJ, Prichard HM, McFall K (2018) Extreme enrichment of selenium in
854 the Apliki Cyprus-type VMS deposit, Troodos, Cyprus. Min Mag 82:697–724

855 Martin AJ, McDonald I, Jenkin GRT, McFall KA, Boyce AJ, Jamieson JW, MacLeod CJ (2021) A
856 missing link between ancient and active mafic-hosted seafloor hydrothermal systems –
857 Magmatic volatile influx in the exceptionally preserved Mala VMS deposit, Troodos, Cyprus.
858 Chem Geol 567:120127

859 Maslennikov VV, Maslennikova SP, Large RR, Danyushevsky LV (2009) Study of Trace Element
860 Zonation in Vent Chimneys from the Silurian Yaman-Kasy Volcanic-Hosted Massive Sulfide
861 Deposit (Southern Urals, Russia) Using Laser Ablation-Inductively Coupled Plasma Mass
862 Spectrometry (LA-ICPMS). Econ Geol 104:1111–1141

863 Mathieu L (2019) Detecting magmatic-derived fluids using pyrite chemistry: Example of the
864 Chibougamau area, Abitibi Subprovince, Québec. Ore Geol Rev 114:103-127

865 McDermott JM, Ono S, Tivey MK, Seewald JS, Shanks WC, Solow AR (2015) Identification of sulfur
866 sources and isotopic equilibria in submarine hot-springs using multiple sulfur isotopes. Geochim
867 Cosmochim Acta 160:169–187

868 McDonald MJ, Piercey SJ, Layne GD, Pigage LC, Piercey G (2018) Mineral Assemblages, Textures and
869 In Situ Sulphur Isotope Geochemistry of Sulphide Mineralization from the Cyprus-Type Ice
870 Volcanogenic Massive Sulphide (VMS) Deposit, Yukon, Canada. Minerals 8:501

871 McPhail DC (1995) Thermodynamic properties of aqueous tellurium species between 25 and 350°.
872 Geochim Cosmochim Acta 59:851–866

873 Melekestseva IY, Tret'yakov GA, Nimis P, Yuminov AM, Maslennikov VV, Maslennikova SP,
874 Kotlyarov VA, Beltenev VE, Danyushevsky LV, Large R (2014) Barite-rich massive sulfides
875 from the Semenov-1 hydrothermal field (Mid-Atlantic Ridge, 13°30.87′ N): Evidence for phase
876 separation and magmatic input. Mar Geol 349:37–54

877 Meng X, Li X, Chu F, Fu B, Lei J, Li Z, Wang H, Chen L (2019) Multi-stage growth and fluid
878 evolution of a hydrothermal sulphide chimney in the East Pacific Ridge 1–2° S hydrothermal
879 field: constraints from in situ sulphur isotopes. Geol Mag 156:989–1002

880 Meng X, Li X, Chu F, Zhu J, Lei J, Li Z, Wang H, Chen L, Zhu Z (2020) Trace element and sulfur
881 isotope compositions for pyrite across the mineralization zones of a sulfide chimney from the
882 East Pacific Rise (1-2°S). Ore Geol Rev 116:103209
883 Monecke T, Petersen S, Hannington MD, Grant H, Samson I (2016) The minor element endowment
884 of modern sea-floor massive sulfides and comparison with deposits hosted in ancient
885 volcanic successions. Rev Econ Geol 18:245-306
886 Muenow DW, Garciat MO, Aggrey KE, Bednarz U, Schmincke HU (1990) Volatiles in submarine
887 glasses as a discriminant of tectonic origin: application to the Troodos ophiolite. Nature 343:
888 159–161
889 Mukasa SB, Ludden JN (1987) Uranium-lead isotopic ages of plagiogranites from the Troodos ophiolite,
890 Cyprus, and their tectonic significance. Geology 15:825–828
891 Murton BJ, Lehrmann B, Dutrieux AM, Martins S, de la Iglesia AG, Stobbs IJ, Barriga FJAS, Bialas J,
892 Dannowski A, Vardy ME, North LJ, Yeo IALM, Lusty PAJ, Petersen S (2019) Geological fate of
893 seafloor massive sulphides at the TAG hydrothermal field (Mid-Atlantic Ridge). Ore Geol Rev
894 107:903–925
895 Ohmoto H (1996) Formation of volcanogenic massive sulfide deposits: The Kuroko perspective. Ore
896 Geol Rev 10:135–177
897 Ohmoto H, Lasaga AC (1982) Kinetics of reactions between aqueous sulfates and sulfides in
898 hydrothermal systems. Geochim Cosmochim Acta 46:1727–1745
899 Ono S, Shanks WC, Rouxel OJ, Rumble D (2007) S-33 constraints on the seawater sulfate contribution in
900 modern seafloor hydrothermal vent sulfides. Geochim Cosmochim Acta 71:1170–1182
901 Parvaz DB, 2014. Oxidation Zones of Volcanogenic Massive Sulphide Deposits in the Troodos Ophiolite,
902 Cyprus: Targeting Secondary Copper Deposits. Doctoral Thesis, University of Exeter
903 Patten CGC, Pitcairn IK, Alt JC, Zack T, Lahaye Y, Teagle DAH, Markdahl, K., 2020. Metal fluxes
904 during magmatic degassing in the oceanic crust: sulfide mineralisation at ODP site 786B, Izu-
905 Bonin forearc. Miner Deposita 55, 469–489

906 Patten CGC, Pitcairn IK, Teagle DAH, (2017) Hydrothermal mobilisation of Au and other metals in
907 supra-subduction oceanic crust: Insights from the Troodos ophiolite. Ore Geol Rev 86:487–508
908 Pearce JA, Robinson PT (2010) The Troodos ophiolitic complex probably formed in a subduction
909 initiation, slab edge setting. Gondwana Res, A Tribute to Miyashiro 18:60–81
910 Pedersen L-ER, Staudigel H, McLoughlin N, Whitehouse MJ, Strauss H (2017) A multiple sulfur isotope
911 study through the volcanic section of the Troodos ophiolite. Chem Geol 46:849–62
912 Petersen S, Herzig PM, Hannington MD (2000) Third dimension of a presently forming VMS deposit:
913 TAG hydrothermal mound, Mid-Atlantic Ridge, 26°N. Miner Deposita 35:233–259
914 Petersen S, Herzig PM, Hannington MD, Jonasson IR, Arribas A (2002) Submarine Gold Mineralization
915 Near Lihir Island, New Ireland Fore-Arc, Papua New Guinea. Econ Geol 97:1795–1813
916 Prichard HM, Knight RD, Fisher PC, McDonald I, Zhou M-F, Wang CY (2013) Distribution of platinum-
917 group elements in magmatic and altered ores in the Jinchuan intrusion, China: an example of
918 selenium remobilization by postmagmatic fluids. Miner Deposita 48:767–786
919 Rautenschlein M, Jenner GA, Hertogen J, Hofmann AW, Kerrich R, Schmincke H-U, White WM (1985)
920 Isotopic and trace element composition of volcanic glasses from the Akaki Canyon, Cyprus:
921 implications for the origin of the Troodos ophiolite. Earth Planet Sci Lett 75:369–383
922 Reed MH, Palandri J (2006) Sulfide Mineral Precipitation from Hydrothermal Fluids. Rev Mineral
923 Geochem 61:609–631
924 Revan MK, Genç Y, Maslennikov VV, Maslennikova SP, Large RR, Danyushevsky LV (2014)
925 Mineralogy and trace-element geochemistry of sulfide minerals in hydrothermal chimneys from
926 the Upper-Cretaceous VMS deposits of the eastern Pontide orogenic belt (NE Turkey). Ore Geol
927 Rev 63:129–149
928 Richardson CJ, Cann JR, Richards HG, Cowan JG (1987) Metal-depleted root zones of the Troodos ore-
929 forming hydrothermal systems, Cyprus. Earth Planet Sci Lett 84:243–253

930 Rouxel O, Fouquet Y, Ludden JN (2004) Subsurface processes at the lucky strike hydrothermal field,
931 Mid-Atlantic ridge: evidence from sulfur, selenium, and iron isotopes. Geochim Cosmochim Acta
932 68:2295–2311
933 Rouxel O, Ono S, Alt J, Rumble D, Ludden J (2008) Sulfur isotope evidence for microbial sulfate
934 reduction in altered oceanic basalts at ODP Site 801. Earth Planet Sci Lett 268:110–123
935 Sakai H (1968) Isotopic properties of sulfur compounds in hydrothermal processes. Geochem J 2:29–49
936 Shanks WC (2001) Stable Isotopes in Seafloor Hydrothermal Systems: Vent fluids, hydrothermal
937 deposits, hydrothermal alteration, and microbial processes. Rev Mineral Geochem 43:469–525
938 Sharman ER, Taylor BE, Minarik WG, Dubé B, Wing BA (2015) Sulfur isotope and trace element data
939 from ore sulfides in the Noranda district (Abitibi, Canada): implications for volcanogenic massive
940 sulfide deposit genesis. Miner Deposita 50:591–606
941 Sillitoe RH, Hannington MD, Thompson JFH (1996) High sulfidation deposits in the volcanogenic
942 massive sulfide environment. Econ Geol 91:204–212
943 Tivey MK (2007) Generation of Seafloor Hydrothermal Vent Fluids and Associated Mineral Deposits.
944 Oceanography 20:50–65
945 Tivey MK, Humphris SE, Thompson G, Hannington MD, Rona PA (1995). Deducing patterns of fluid
946 flow and mixing within the TAG active hydrothermal mound using mineralogical and
947 geochemical data. J Geophys Res Solid Earth 100:12527–12555.
948 Varga RJ, Moores EM (1985) Spreading structure of the Troodos ophiolite, Cyprus. Geology 13:846–
949 850.
950 Von Damm KL, Oosting SE, Kozlowski R, Buttermore LG, Colodner DC, Edmonds HN, Edmond JM,
951 Grebmeier JM (1995) Evolution of East Pacific Rise hydrothermal vent fluids following a
952 volcanic eruption. Nature 375:47–50
953 Von Damm KL (1995) Controls on the Chemistry and Temporal Variability of Seafloor Hydrothermal
954 Fluids. In: SE Humphris, Zierenberg RA, Mullineaux LS, Thomson RE (ed) Seafloor

955 Hydrothermal Systems: Physical, Chemical, Biological, and Geological Interactions. American
956 Geophysical Union, Washington D.C., vol.91 pp. 222–247
957 Wang Y, Han X, Petersen S, Frische M, Qiu Z, Cai Y, Zhou P (2018) Trace Metal Distribution in Sulfide
958 Minerals from Ultramafic-Hosted Hydrothermal Systems: Examples from the Kairei Vent Field,
959 Central Indian Ridge. Minerals 8:526
960 Woelki D, Regelous M, Haase KM, Romer RHW, Beier C (2018) Petrogenesis of boninitic lavas from
961 the Troodos Ophiolite, and comparison with Izu–Bonin–Mariana fore-arc crust. Earth Planet Sci
962 Lett. 498:203–214
963 Wohlgemuth-Ueberwasser CC, Viljoen F, Petersen S, Vorster C (2015) Distribution and solubility limits
964 of trace elements in hydrothermal black smoker sulfides: An in-situ LA-ICP-MS study. Geochim
965 Cosmochim Acta 159:16–41
966 Woodruff LG, Shanks WC (1988) Sulfur isotope study of chimney minerals and vent fluids from 21°N,
967 East Pacific Rise: Hydrothermal sulfur sources and disequilibrium sulfate reduction. J Geophys
968 Res Solid Earth 93:4562–4572
969 Wortmann UG, Bernasconi SM, Böttcher ME (2001) Hypersulfidic deep biosphere indicates extreme
970 sulfur isotope fractionation during single-step microbial sulfate reduction. Geology 29:647-650
971 Yamamoto M (1976) Relationship between Se/S and sulfur isotope ratios of hydrothermal sulfide
972 minerals. Mineral Deposita 11:197–209
973 Yang K, Scott SD (2002) Magmatic Degassing of Volatiles and Ore Metals into a Hydrothermal System
974 on the Modern Sea Floor of the Eastern Manus Back-Arc Basin, Western Pacific. Econ Geol 97:
975 1079–1100
976 Yang K, Scott SD (1996) Possible contribution of a metal-rich magmatic fluid to a sea-floor hydrothermal
977 system. Nature 383:420–423
978 Yeats CJ, Parr JM, Binns RA, Gemmell JB, Scott SD (2014) The SuSu Knolls Hydrothermal Field,
979 Eastern Manus Basin, Papua New Guinea: An Active Submarine High-Sulfidation Copper-Gold
980 System. Econ Geol 109:2207–2226

You C-F, Bickle MJ (1998) Evolution of an active sea-floor massive sulphide deposit. Nature 394:668–671

Zeng Z, Ma Y, Chen S, Selby D, Wang X, Yin X (2017) Sulfur and lead isotopic compositions of massive sulfides from deep-sea hydrothermal systems: Implications for ore genesis and fluid circulation. Ore Geol Rev 87:155–171

Figure Captions

Figure 1: Simplified geological map of the Troodos ophiolite, Cyprus. Graben axes are indicated by the dashed lines. Mala is located in the SW of the ophiolite at the LPL/BG transitional horizon (after Martin et al. 2018).

Figure 2: Field observations from the Mala VMS deposit. A) The exposed portion of the Mala mound. The VMS mound contains pyrite and crudely layered gypsum capped by a veneer of leached volcanic rocks. The margin of the VMS mound is denoted by the white dashed line. B) Coarse-grained euhedral pyrite with infilling gypsum (white). C) Massive pyrite. D) Massive gypsum horizon located in the upper mound region containing coarse (1-2 cm) euhedral pyrite grains. E) Gypsum containing finely disseminated euhedral pyrite. F) Euhedral pyrite in a gypsum matrix with minor Fe oxide staining. G) Aggregates of euhedral pyrite in gypsum.

Figure 3: Photomicrographs in reflected light of common pyrite textures at Mala. A) Massive pyrite. Note porous inclusion trails delineating crystal growth zones. B) The relationship between massive and dendritic pyrite textures. C) Dendritic pyrite. D) Colloform pyrite in a matrix of porous pyrite. E) Granular pyrite consisting of anhedral rounded pyrite in a matrix of Fe-oxides and pyrite. F) Finely disseminated euhedral to subhedral pyrite in surrounding altered volcanic rocks.

Figure 4: Pyrite chemistry analysed via LA-ICP-MS. Pyrite analyses are divided based on grain morphology into disseminated (n=78), massive (n=40), granular (n=10) and colloform (n=15). Analyses that are below detection limit are excluded (Table S1, ESM). A) Te vs. Co, B) Te vs. Se, C) Co vs. Se. D) Total measured

trace metal by pyrite texture (Co, Ni, Cu, Zn, As, Se, Ag, Cd, Sb, Te, Re, Au, Pb and Bi). Data in ESM, Table S1.

Figure 5: Pyrite chemistry analysed via LA-ICP-MS from the core (n=35) and rim (n=43) of individual disseminated pyrite grains. The rim of pyrite grains are enriched in Co and Cu and relative to the margin. Data in ESM, Table S1.

Figure 6: Summary of sulfur isotope analyses ($\delta^{34}S$) analysed by SIMS (n=31) and classified based on pyrite texture. Massive pyrite exhibits the largest range in its $\delta^{34}S$ composition whilst colloform pyrite clusters between 0 and -5‰. Data and standard information in ESM, Table S3.

Figure 7: SIMS spot analyses across disseminated pyrite grains. Lower images are the same grain etched with NaOCl to reveal any internal zonations. A) Sample MAL 05 (in the lower image "SG" refers to different sub-grains), B) sample MAL 11-A, C) MAL 11-B.

Figure 8: LA-ICP-MS analyses for individual mineral grains. A) Se vs. As, B) Se vs. Te, C) Se vs. Co. Data in Table S1 and sample description in Figure S1, ESM.

Figure 9: A comparison between bulk $\delta^{34}S$ analyses of Mala samples (Martin et al. 2021) with the same sub-set of samples analysed by SIMS in this study. Samples analysed by SIMS exhibit notably more variation with extremely low (-17.1‰) and high (7.5‰) values compared to the samples analysed using bulk methods. Cretaceous seawater 18 to 19‰ (SW) (Kampschulte and Strauss 2004) and Troodos magmatic mean 0 to 1‰ (TO magmatic mean; Alt 1994).

Figure 10: Coupled trace metal and $\delta^{34}S$ analyses across individual disseminated pyrite grains. A) Sample MAL 05. B) Sample MAL 11 A. C) Sample MAL 11 B. P1 on X axis refers to the specific analytical point in the image above. Selenium, As, Co and Te concentrations are shown by red lines with corresponding concentration in ppm on the secondary axis (right). Note varying Y axis between graphs.

Figure 11: Se, Te and Co vs. $\delta^{34}S$ for all samples. Twinned points in disseminated pyrite (as in Fig. 10) are represented by multiple analytical points. In samples where points were not twinned an average value is reported and denoted by * next to each sample in the legend. A) Se vs. $\delta^{34}S$, B) Te vs. $\delta^{34}S$, C) Co vs. $\delta^{34}S$. Volatile trend in plot B shows expected trend between Te, Se and Co and $\delta^{34}S$. The grey box represents the primary magmatic mean for Troodos magmatic rocks (Alt 1994). Solid line represents the average bulk $\delta^{34}S$ for all Troodos VMS (4.6‰; Martin et al. 2020) and the dashed line is the bulk median $\delta^{34}S$ for Mala (-4.3‰; Martin et al. 2021).

Figure 12: A) Summary schematic for mound scale metal enrichment processes at the Mala VMS deposit. Granular pyrite forms from the reworking and collapse of the outer mound and chimney material, metals are remobilized during low temperature fluid flow. Disseminated pyrite forms in gypsum veins and volcanic rocks (Fig. 2). B) Colloform and dendritic textured pyrite (Fig. 3 C and D) form at the margin of the sulfide mound where seawater ingress is high creating disequilibrium textures and fluid temperatures are lower (<350°C) leading to an enrichment in Ag, Au and Pb. C) With increasing time, permeability pathways within the mound change in response to the collapse and reworking of anhydrite, creating a prominent brecciated texture leading to localised zone refining on the cm/m scale in response to new high temperature fluid pathways. D) Pyrite grains undergo zone refining leading to the decoupling of $\delta^{34}S$ and magmatic volatile elements in pyrite.

Table Captions

Table 1: Summary of pyrite geochemistry classified by texture: colloform (n=15), granular (n=10), massive (n=40) and disseminated (n=78). Points that were below detection limit (Table S1 and S2, ESM) are excluded (n > DL = number of analyses above detection limit).

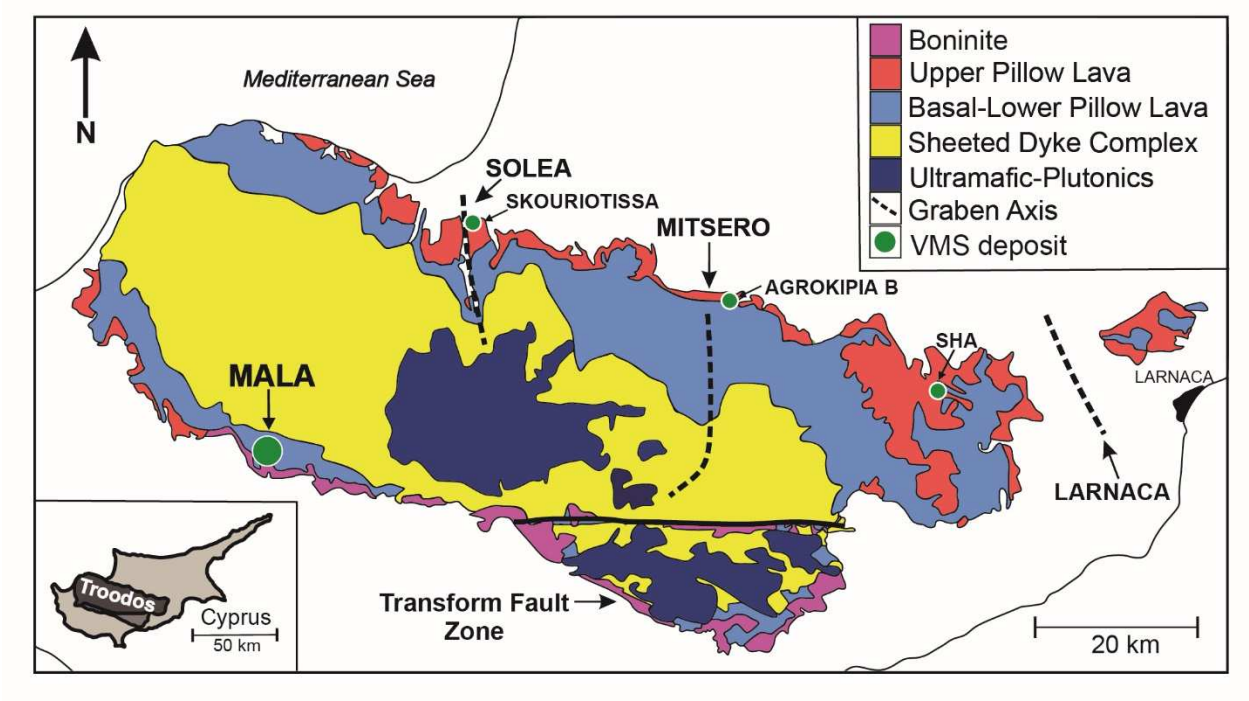
N
Mediterranean Sea
SOLEA
SKOURIOTISSA
MITSERO
AGROKIPIA B
SHA
MALA
LARNACA
LARNACA
Boninite
Upper Pillow Lava
Basal-Lower Pillow Lava
Sheeted Dyke Complex
Ultramafic-Plutonics
Graben Axis
VMS deposit
Troodos
Cyprus
50 km
Transform Fault Zone
20 km

1050

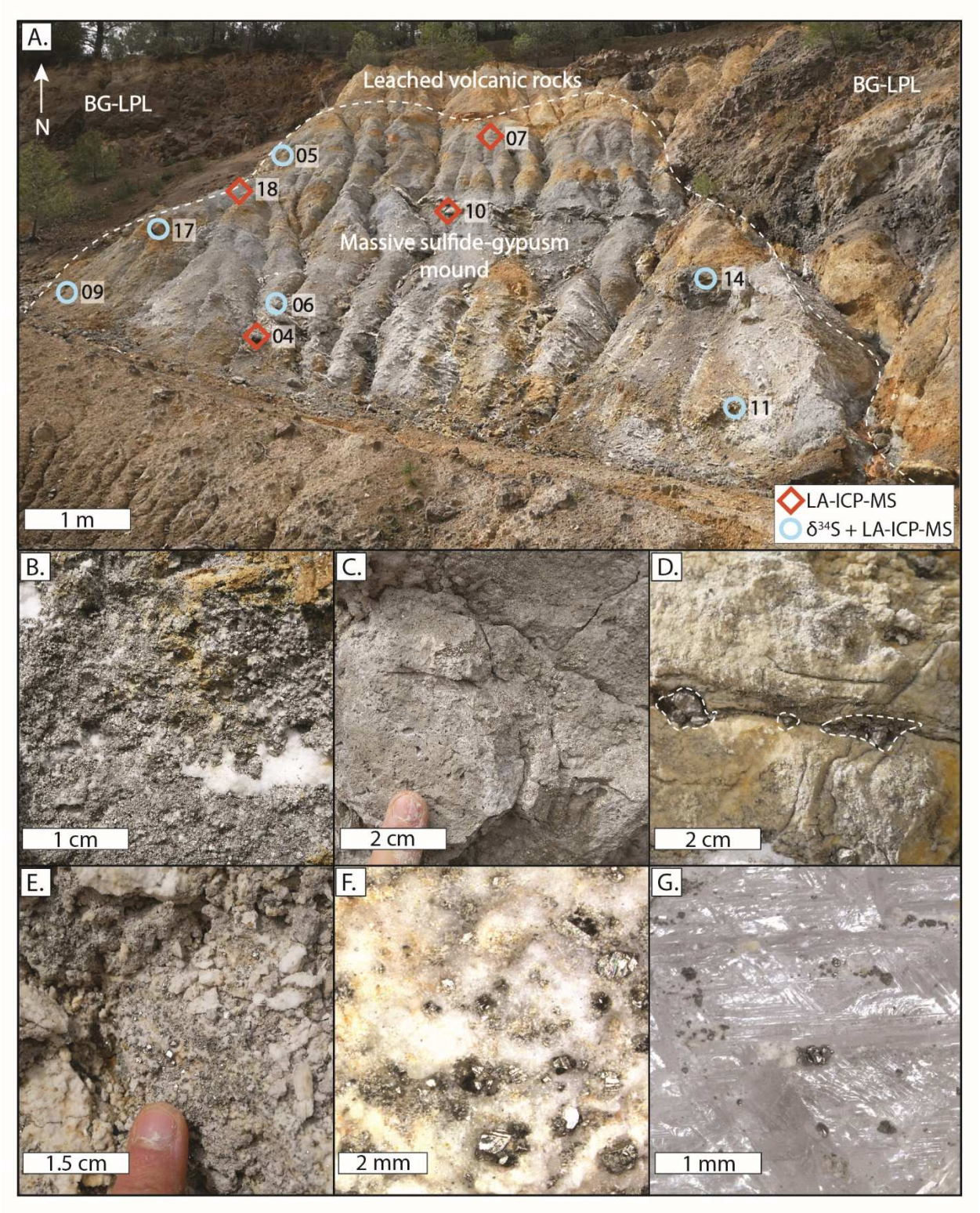
A.
N
BG-LPL
Leached volcanic rocks
BG-LPL
07
05
18
10
17
Massive sulfide-gypsum mound
14
09
06
04
11
1 m
LA-ICP-MS
δ34S + LA-ICP-MS
B.
1 cm
C.
2 cm
D.
2 cm
E.
1.5 cm
F.
2 mm
G.
1 mm

1051

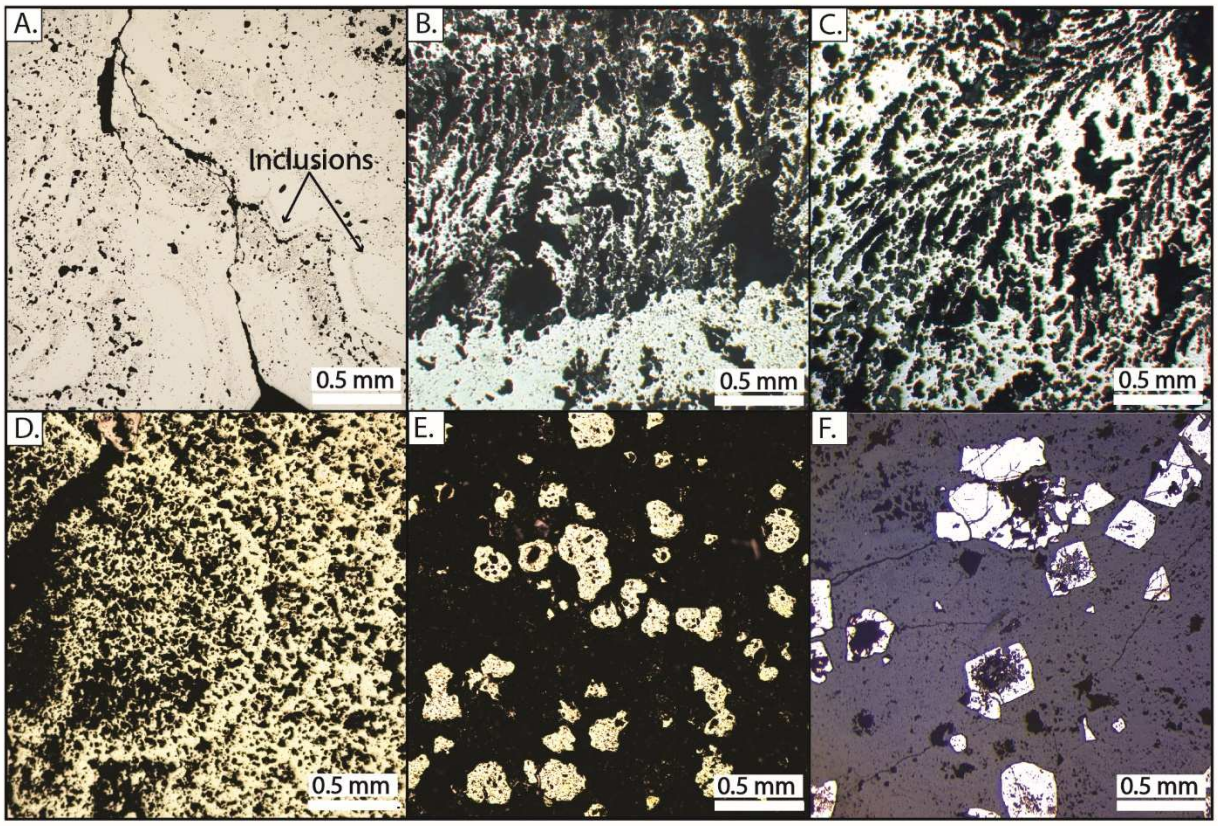

1052

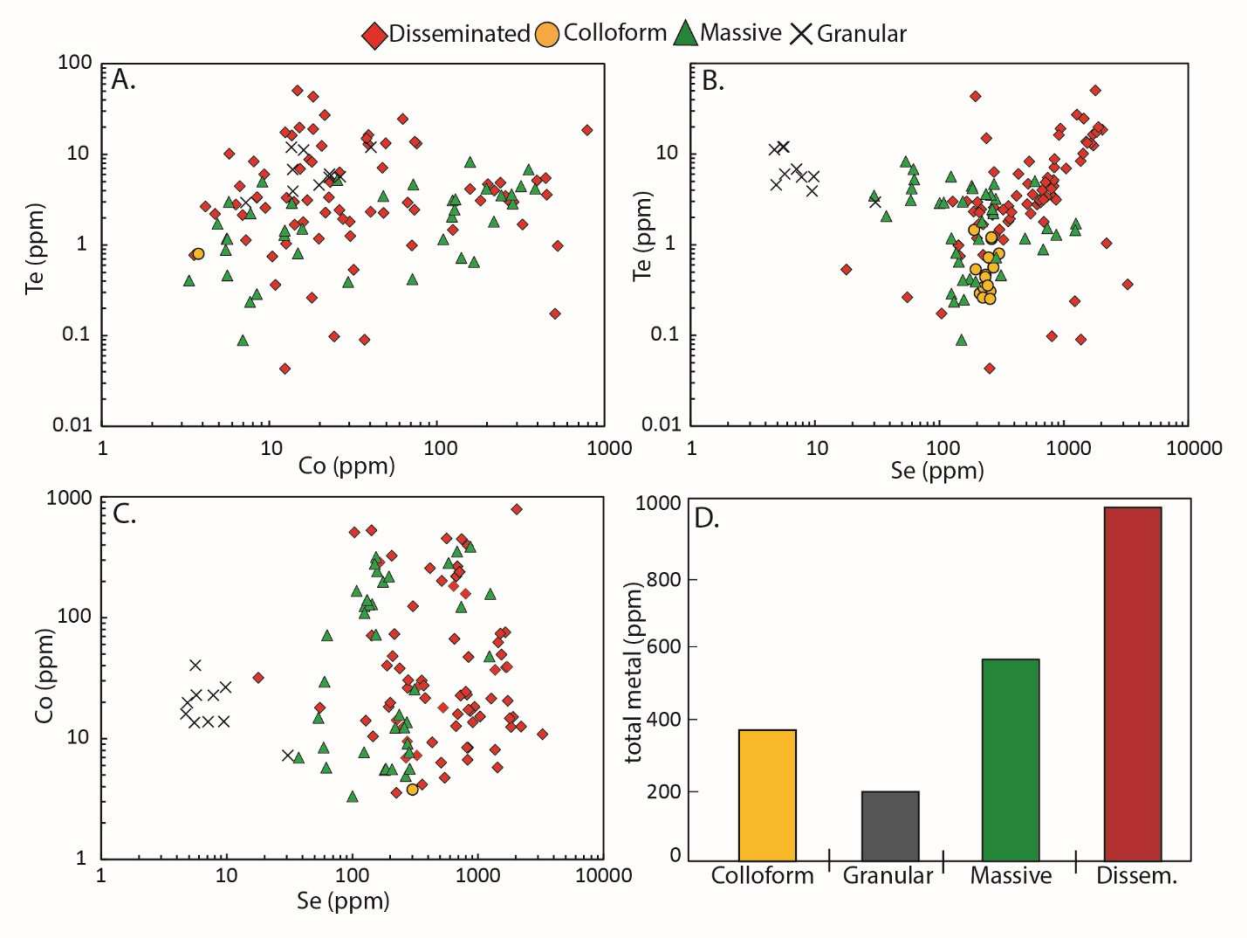

1053

1054

1055

1056

1057

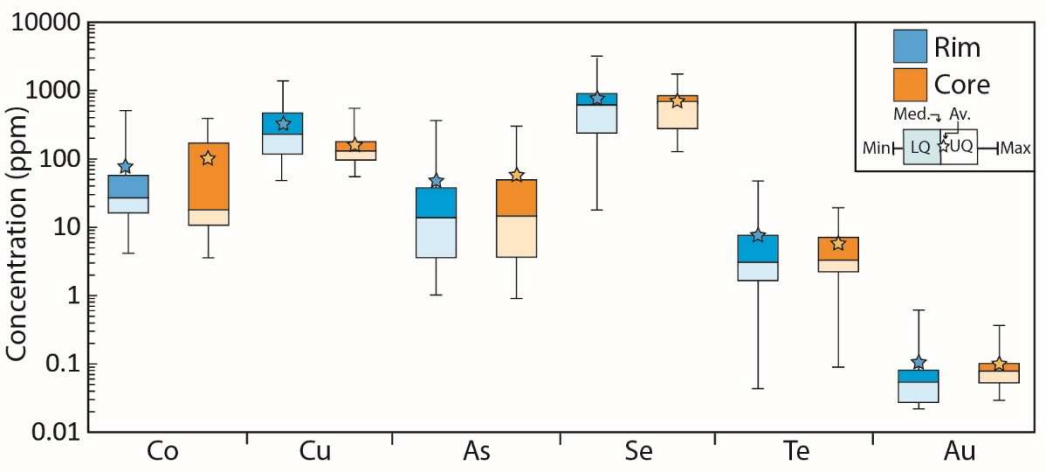

1058

1059

1060

1061

1062

1063

1064

1065

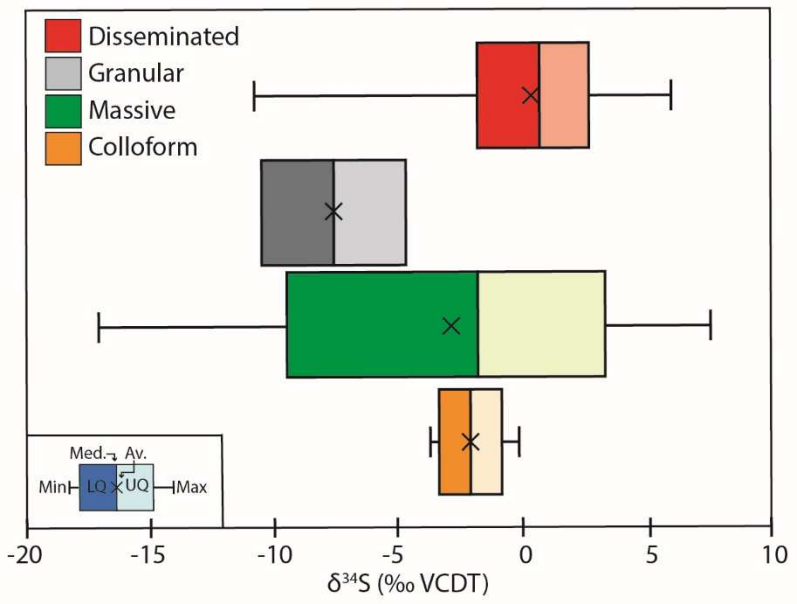

1066

1067

1068

1069

1070

1071

1072

1073

1074

1075

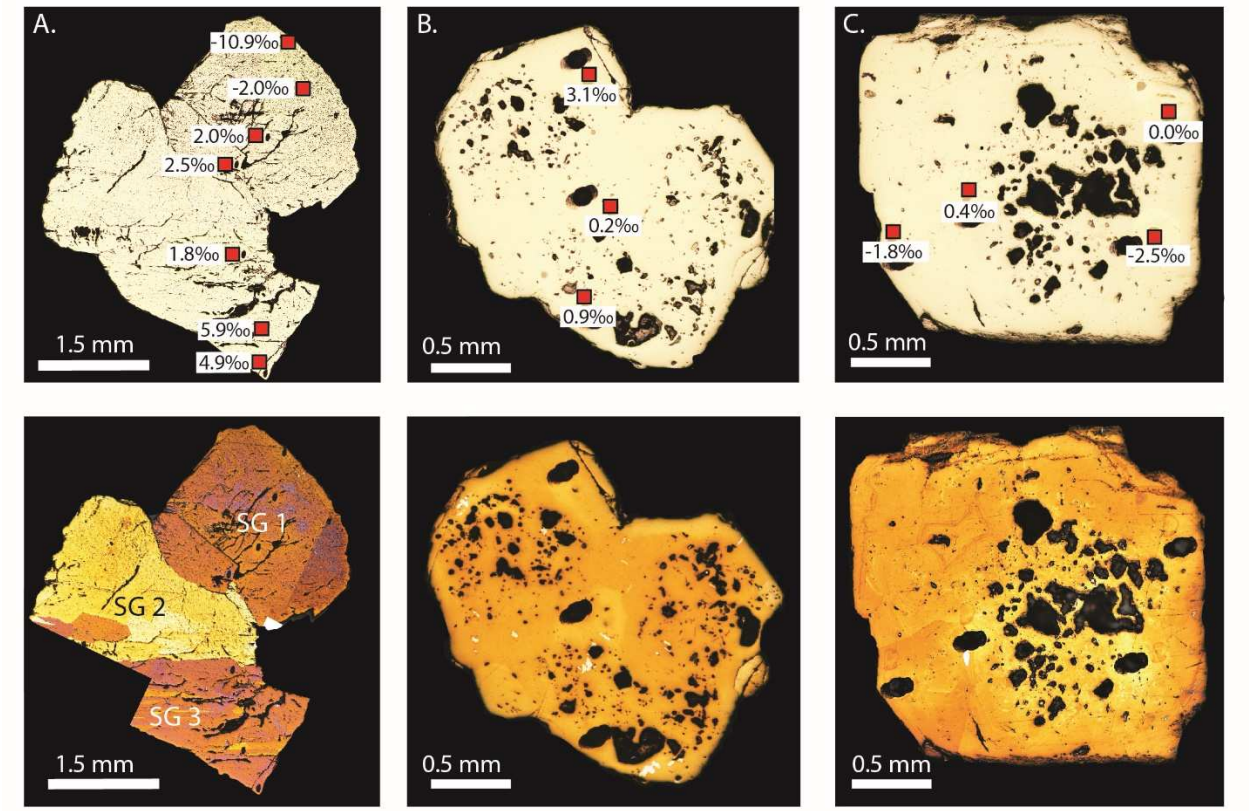

1076

1077

1078

1079

1080

1081

1082

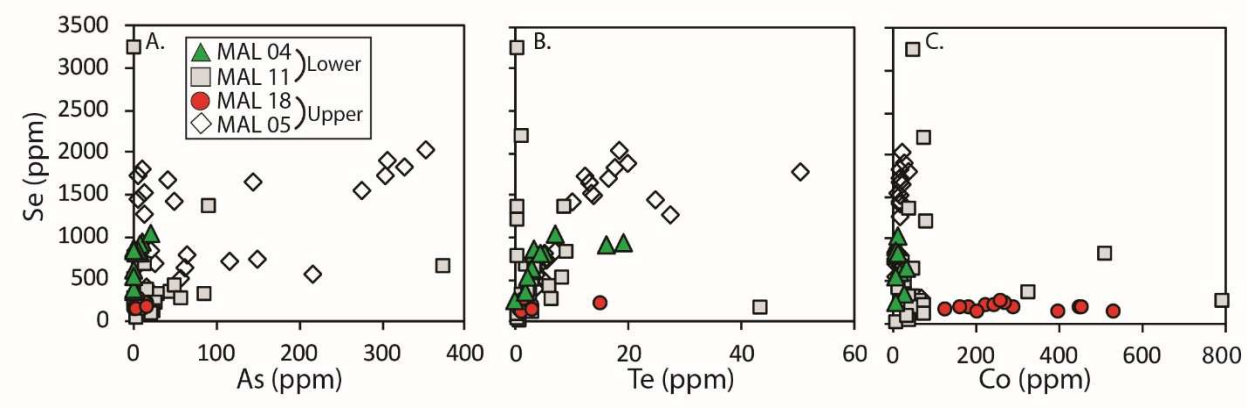

1083

1084

1085

1086

1087

1088

1089

1090

1091

1092

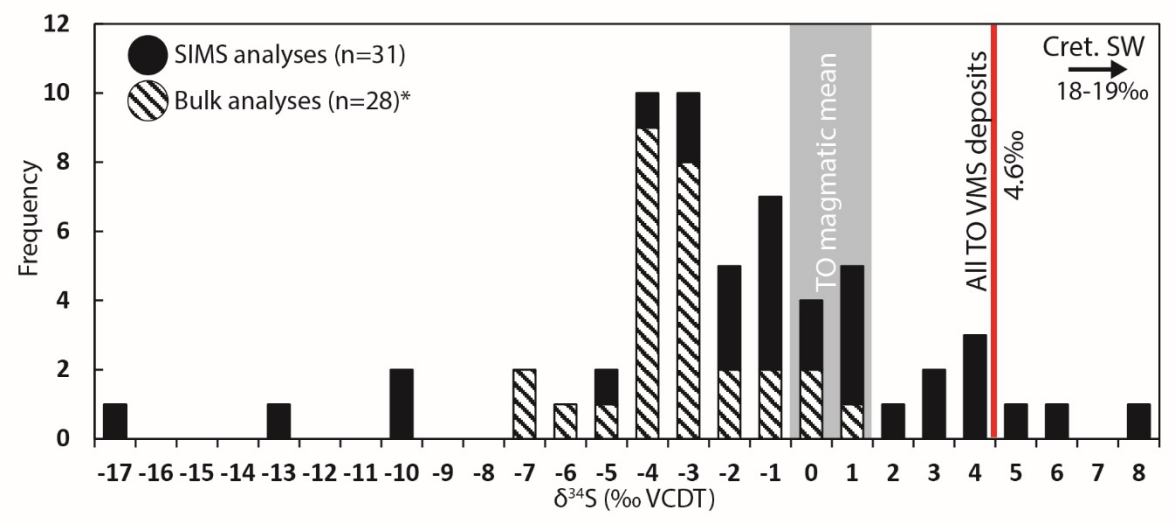
SIMS analyses (n=31)
Bulk analyses (n=28)*
TO magmatic mean
All TO VMS deposits
4.6‰
Cret. SW
18-19‰
Frequency
δ34S (‰ VCDT)

1093

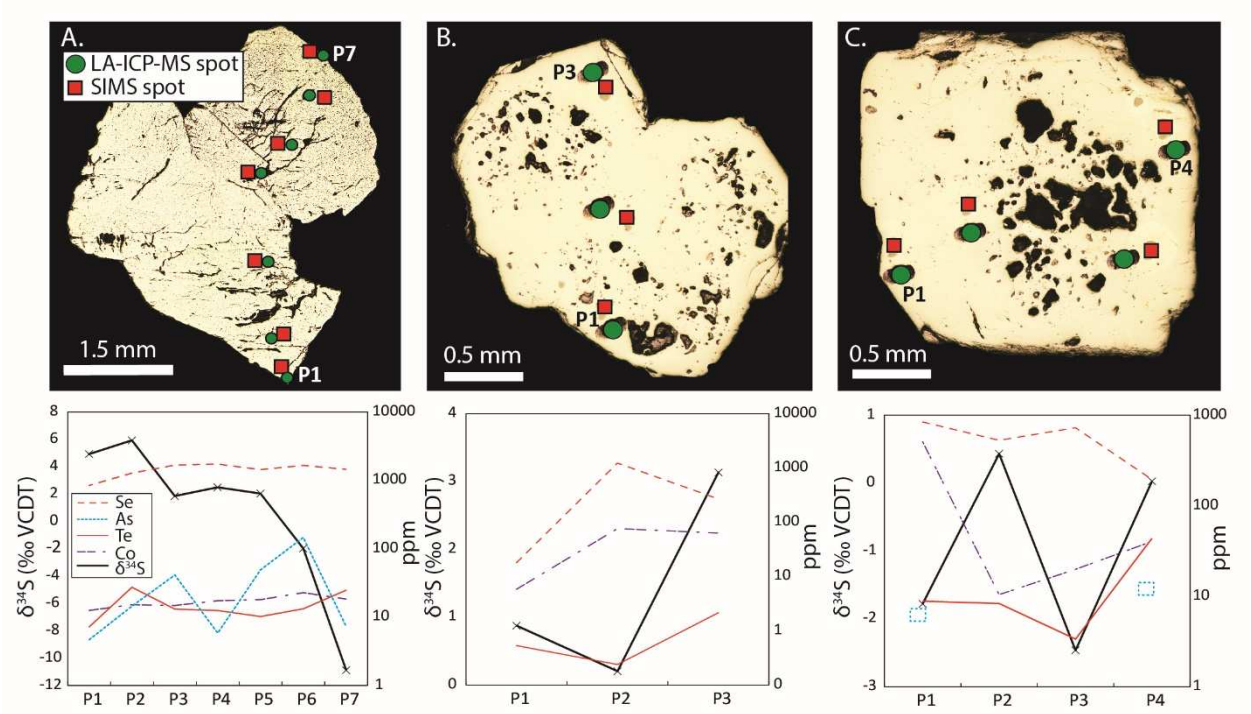
A.
LA-ICP-MS spot
SIMS spot
P7
P1
1.5 mm
B.
P3
P1
0.5 mm
C.
P4
P1
0.5 mm
δ34S (‰ VCDT)
ppm
Se
As
Te
Co
δ34S
P1 P2 P3 P4 P5 P6 P7
P1 P2 P3
P1 P2 P3 P4

1094

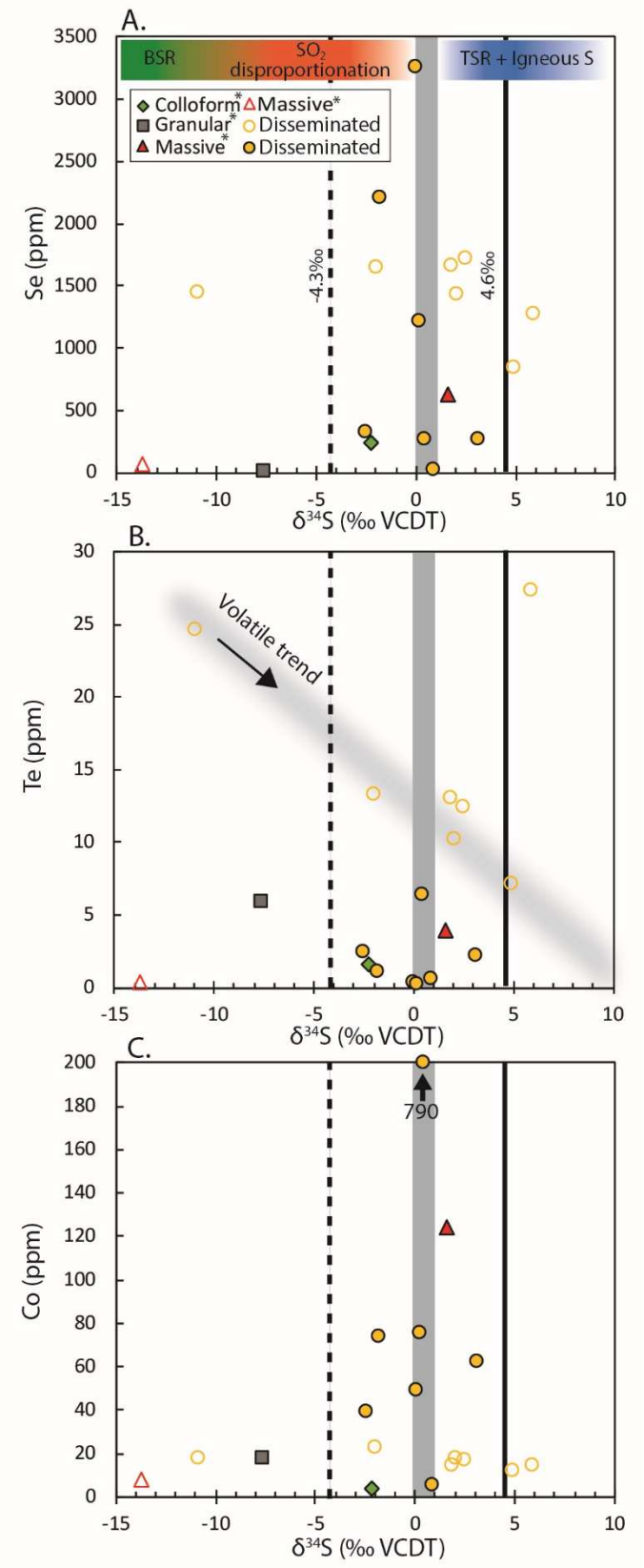
A.
BSR
SO2 disproportionation
TSR + Igneous S
Colloform*
Granular*
Massive*
Massive*
Disseminated
Disseminated
-4.3‰
4.6‰
Se (ppm)
δ34S (‰ VCDT)
B.
Volatile trend
Te (ppm)
δ34S (‰ VCDT)
C.
790
Co (ppm)
δ34S (‰ VCDT)

1095

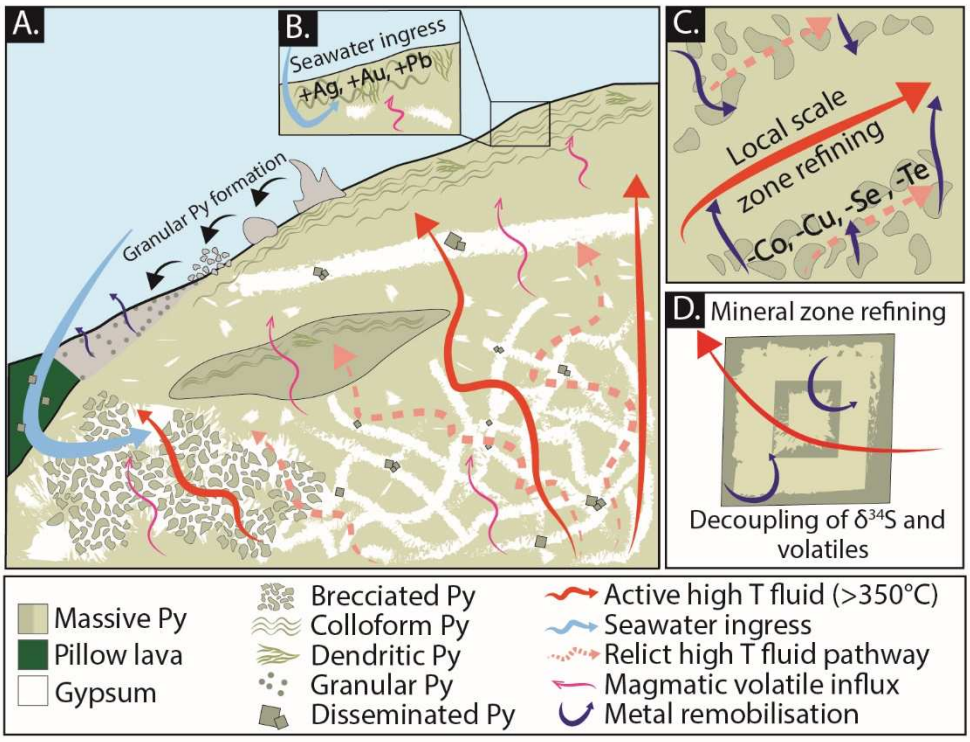
A.
B.
Seawater ingress
+Ag, +Au, +Pb
Granular Py formation
C.
Local scale
zone refining
-Co, -Cu, -Se, -Te
D. Mineral zone refining
Decoupling of δ34S and volatiles
Massive Py
Pillow lava
Gypsum
Brecciated Py
Colloform Py
Dendritic Py
Granular Py
Disseminated Py
Active high T fluid (>350°C)
Seawater ingress
Relict high T fluid pathway
Magmatic volatile influx
Metal remobilisation

1096

		Colloform				Granular				Massive				Disseminated			
		Median	Min	Max	n > DL	Median	Min	Max	n > DL	Median	Min	Max	n > DL	Median	Min	Max	n > DL
Co	ppm			3.78	1	17.9	7.25	40.5	10	38.8	3.33	386.5	38	23.1	3.56	789.6	75
Ni	wt.%				0				0			0.01	1	0.01	0.01	0.07	12
Cu	wt.%	0.01	0.01	0.13	4		0.01	0.02	2	0.02	0.01	0.11	13	0.02	0.01	0.15	31
Zn	ppm		6.73	9.01	2				0	11.2	9.44	38.8	5	14.04	10.0	17.7	8
As	ppm	4.18	1.55	24.0	15	2.84	1.37	4.72	7	3.14	1.18	94.7	26	13.6	0.90	373.6	68
Se	ppm	244.6	195.9	301.7	15	6.40	4.72	30.6	10	178.3	29.8	1252.7	40	644.9	17.9	3260.7	78
Ag	ppm	0.24	0.15	0.49	15				0	0.42	0.16	0.89	11	0.24	0.19	0.33	7
Cd	ppm				0				0			0.26	1			0.67	1
Sb	ppm	0.47	0.25	1.46	15			0.35	1	0.97	0.16	5.76	14	0.25	0.22	1.14	3
Te	ppm	1.51	0.86	3.13	15	5.86	2.94	12.0	10	1.76	0.09	8.30	40	3.14	0.04	50.6	78
Re	ppm	0.17	0.11	0.25	15				0	0.15	0.03	0.83	17	0.05	0.01	1.80	35
Au	ppm	0.13	0.08	0.25	15		0.03	0.03	2	0.06	0.02	0.24	24	0.06	0.01	0.60	24
Pb	ppm	9.83	6.94	15.1	15				0	7.01	3.25	46.5	13	5.27	0.49	25.6	8
Bi	ppm	0.05	0.03	0.12	15			0.03	1	0.08	0.03	0.26	22	0.12	0.03	0.47	19

1097